

Lawrence Berkeley National Laboratory

Lawrence Berkeley National Laboratory

Title

Characterization of the effects of x-ray irradiation on the hierarchical structure and mechanical properties of human cortical bone

Permalink

<https://escholarship.org/uc/item/0rf53907>

Author

Barth, Holly

Publication Date

2011-12-01

Peer reviewed

Manuscript Number: jbmt17976R1

Title: Characterization of the effects of x-ray irradiation on the hierarchical structure and mechanical properties of human cortical bone

Article Type: FLA Original Research

Section/Category: Biomaterials and Regenerative Medicine (BRM)

Keywords: Human cortical bone; x-ray radiation; deformation; toughness; collagen; x-ray diffraction; tomography

Corresponding Author: Dr. Robert Oliver Ritchie, MA, PhD, ScD

Corresponding Author's Institution: University of California at Berkeley

First Author: Holly D Barth

Order of Authors: Holly D Barth; Elizabeth A Zimmermann; Eric Schaible; Simon Y Tang; Tamara Alliston; Robert Oliver Ritchie, MA, PhD, ScD

Abstract: Bone comprises a complex structure of primarily collagen, hydroxyapatite and water, where each hierarchical structural level contributes to its strength, ductility and toughness. These properties, however, are degraded by irradiation, arising from medical therapy or bone-allograft sterilization. We provide here a mechanistic framework for how irradiation affects the nature and properties of human cortical bone over a range of characteristic (nano to macro) length-scales, following x-ray exposures up to 630 kGy. Macroscopically, bone strength, ductility and fracture resistance are seen to be progressively degraded with increasing irradiation levels. At the micron-scale, fracture properties, evaluated using in-situ scanning electron microscopy and synchrotron x-ray computed micro-tomography, provide mechanistic information on how cracks interact with the bone-matrix structure. At sub-micron scales, strength properties are evaluated with in-situ tensile tests in the synchrotron using small-/wide-angle x-ray scattering/diffraction, where strains are simultaneously measured in the macroscopic tissue, collagen fibrils and mineral. Compared to healthy bone, results show that the fibrillar strain is decreased by ~40% following 70 kGy exposures, consistent with significant stiffening and degradation of the collagen. We attribute the irradiation-induced deterioration in mechanical properties to mechanisms at multiple length-scales, including changes in crack paths at micron-scales, loss of plasticity from suppressed fibrillar sliding at sub-micron scales, and the loss and damage of collagen at the nano-scales, the latter being assessed using Raman and Fourier-Transform-Infrared spectroscopy and a fluorometric assay.

UNIVERSITY OF CALIFORNIA, BERKELEY

BERKELEY · DAVIS · IRVINE · LOS ANGELES · RIVERSIDE · SAN DIEGO · SAN FRANCISCO



SANTA BARBARA · SANTA CRUZ

DEPARTMENT OF MATERIALS SCIENCE
AND ENGINEERING

Robert O. Ritchie, Ph.D., Sc.D. (Cantab.)
H.T. & Jessie Chua Distinguished Professor of Engineering
Professor of Materials Science & Engineering
Professor of Mechanical Engineering

216 HEARST MEMORIAL MINING BLDG.
BERKELEY, CALIFORNIA 94720-1760
tel: (510) 486-5798
cell: (510) 409-1779
fax: (510) 643-5792
email: RORitchie@LBL.gov
web: <http://www.lbl.gov/Ritchie>

August 5, 2011

Professor D.F. Williams, *FREng*
Editor-in-Chief, *Biomaterials*
biomaterials@online.be

Dear David:

Re: Ms. No. *jmbt17976* "Characterization of the effects of x-ray irradiation on the hierarchical structure and mechanical properties of human cortical bone" by H. D. Barth, E. A. Zimmermann, E. Schaible, S. Y. Tang, T. Alliston and R. O. Ritchie

Thank you for your rapid review of our paper, "Characterization of the effects of x-ray irradiation on the hierarchical structure and mechanical properties of human cortical bone".

We have made changes to the manuscript exactly as you suggested; these are listed below. We are now resubmitting the manuscript in revised form. We hope that you will find it now acceptable for publication in *Biomaterials*.

All the authors have seen and approved the manuscript being resubmitted. The work is original and has not been submitted elsewhere. As corresponding author, I continue to take full responsibility for the submission.

I would be grateful if you could continue to direct all correspondence concerning this manuscript directly to my attention.

My best regards,

A handwritten signature in blue ink, appearing to read "R. O. Ritchie", is written over a light blue horizontal line.

Robert O. Ritchie
Chua Distinguished Professor

Response to Review:

1. Please delete the last paragraph of the Introduction since, in this journal, the Introduction should not give or discuss the results of the work.

The last paragraph of the Introduction has been deleted.

2. Delete 'Taken together' from the last paragraph of the Discussion

The term "Taken together" has been deleted.

3. You have to re-write the Conclusions section. This should not be an extended discussion, but a summary of the main findings and their significance. If there is any discussion in your present Conclusions that has not been included elsewhere you may transfer it to the Discussions section.

The Conclusions have been re-written and shortened somewhat.

4. In the references you should use the accepted abbreviated form for the journal titles - you are inconsistent with this. These can be found in standard databases such as PubMed.

All journal titles in the reference list have now been written in their accepted abbreviated form.

AUTHOR DECLARATION TEMPLATE

We the undersigned declare that this manuscript is original, has not been published before and is not currently being considered for publication elsewhere.

We wish to confirm that there are no known conflicts of interest associated with this publication and there has been no significant financial support for this work that could have influenced its outcome.


We confirm that the manuscript has been read and approved by all named authors and that there are no other persons who satisfied the criteria for authorship but are not listed. We further confirm that the order of authors listed in the manuscript has been approved by all of us.

We confirm that we have given due consideration to the protection of intellectual property associated with this work and that there are no impediments to publication, including the timing of publication, with respect to intellectual property. In so doing we confirm that we have followed the regulations of our institutions concerning intellectual property.

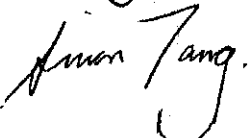
We understand that the Corresponding Author is the sole contact for the Editorial process (including Editorial Manager and direct communications with the office). He/she is responsible for communicating with the other authors about progress, submissions of revisions and final approval of proofs. We confirm that we have provided a current, correct email address which is accessible by the Corresponding Author and which has been configured to accept email from biomaterials@online.be.

Signed by all authors as follows:

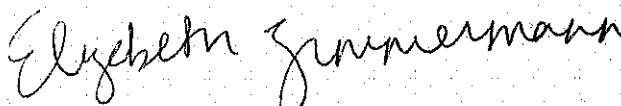
[LIST AUTHORS AND DATED SIGNATURES ALONGSIDE]


Eric Schaible  7/20/11

Holly Barth  7/20/11

Simon Tang  7-21-11

TAMARA ALLISTON  7/21/11

Elizabeth
Zimmermann  7/21/11

ROBERT O. RITCHIE  7/21/11

AUTHOR DECLARATION TEMPLATE

We the undersigned declare that this manuscript is original, has not been published before and is not currently being considered for publication elsewhere.

We wish to confirm that there are no known conflicts of interest associated with this publication and there has been no significant financial support for this work that could have influenced its outcome.

We confirm that the manuscript has been read and approved by all named authors and that there are no other persons who satisfied the criteria for authorship but are not listed. We further confirm that the order of authors listed in the manuscript has been approved by all of us.


We confirm that we have given due consideration to the protection of intellectual property associated with this work and that there are no impediments to publication, including the timing of publication, with respect to intellectual property. In so doing we confirm that we have followed the regulations of our institutions concerning intellectual property.

We understand that the Corresponding Author is the sole contact for the Editorial process (including Editorial Manager and direct communications with the office). He/she is responsible for communicating with the other authors about progress, submissions of revisions and final approval of proofs. We confirm that we have provided a current, correct email address which is accessible by the Corresponding Author and which has been configured to accept email from biomaterials@online.be.

Signed by all authors as follows:

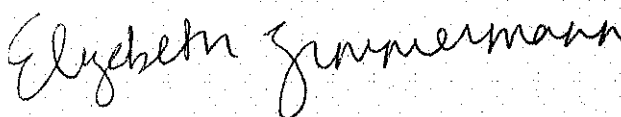
[LIST AUTHORS AND DATED SIGNATURES ALONGSIDE]

Eric Schaible  7/20/11

Holly Barth  7/20/11

Simon Tang  7-21-11

TAMARA ALLISTON  7/21/11

Elizabeth
Zimmermann  7/21/11

ROBERT O. RITCHIE  7/21/11

1
2
3
4
5
6
7
8
9
10
11
12
13
14

Characterization of the effects of x-ray irradiation on the hierarchical structure and mechanical properties of human cortical bone

15
16
17
18
19
20
21
22
23
24
25
26
27
28
29
30
31
32
33
34
35
36
37
38
39
40
41
42
43
44
45
46
47
48
49
50
51
52
53
54
55
56

H. D. Barth^{a,b,c}, E. A. Zimmermann^{a,c}, E. Schaible^b, S. Y. Tang^d, T. Alliston^d,
R. O. Ritchie^{a,c,*}

^a*Materials Sciences Division, Lawrence Berkeley National Laboratory, Berkeley, CA, USA*

^b*Experimental Systems Group, Lawrence Berkeley National Laboratory, Berkeley, CA, USA*

^c*Department of Materials Science & Engineering, University of California, Berkeley, CA, USA*

^d*Department of Orthopaedic Surgery, University of California, San Francisco, CA, USA*

57
58
59
60
61
62
63
64
65

*Corresponding author. Department of Materials Science and Engineering, University of California, Berkeley, CA, USA. Tel: +1-510-486-5798; fax: +1-510-643-5792.

E-mail address: RORitchie@lbl.gov (R.O. Ritchie)

1
2
3
4
5
6
7
8
9
10
11
12
13
14
15
16
17
18
19
20
21
22
23
24
25
26
27
28
29
30
31
32
33
34
35
36
37
38
39
40
41
42
43
44
45
46
47
48
49
50
51
52
53
54
55
56
57
58
59
60
61
62
63
64
65

Bone comprises a complex structure of primarily collagen, hydroxyapatite and water, where each hierarchical structural level contributes to its strength, ductility and toughness. These properties, however, are degraded by irradiation, arising from medical therapy or bone-allograft sterilization. We provide here a mechanistic framework for how irradiation affects the nature and properties of human cortical bone over a range of characteristic (nano to macro) length-scales, following x-ray exposures up to 630 kGy. Macroscopically, bone strength, ductility and fracture resistance are seen to be progressively degraded with increasing irradiation levels. At the micron-scale, fracture properties, evaluated using *in-situ* scanning electron microscopy and synchrotron x-ray computed micro-tomography, provide mechanistic information on how cracks interact with the bone-matrix structure. At sub-micron scales, strength properties are evaluated with *in-situ* tensile tests in the synchrotron using small-/wide-angle x-ray scattering/diffraction, where strains are simultaneously measured in the macroscopic tissue, collagen fibrils and mineral. Compared to healthy bone, results show that the fibrillar strain is decreased by ~40% following 70 kGy exposures, consistent with significant stiffening and degradation of the collagen. We attribute the irradiation-induced deterioration in mechanical properties to mechanisms at multiple length-scales, including changes in crack paths at micron-scales, loss of plasticity from suppressed fibrillar sliding at sub-micron scales, and the loss and damage of collagen at the nano-scales, the latter being assessed using Raman and Fourier-Transform-Infrared spectroscopy and a fluorometric assay.

1. Introduction

Bone is a natural composite of organic, mineral and water assembled in the form of a complex hierarchical structure [1]. At the molecular level, it comprises a network of polymetric proteins, primarily type I collagen, with hard and stiff mineral nanoparticles of hydroxyapatite that reinforce it. At sub-micron levels, the collagen forms fibrils (~100 nm diameter) with mineral platelets assembled and periodically spaced on the inside and on the fibril surface; at the micron-scale such fibrils are twisted together to form collagen fibers. At even coarser scales on the order of 10 to 100s μm , human bone's characteristic structure consists of osteons, which are concentric layers of lamellar bone, ~100 μm in diameter, that contain a central, longitudinal, tubular cavity (Haversian canal), blood vessels, and nerves, and which represent a functional unit by which the physical and biological homeostasis of bone is actively maintained.

The stiffness, strength and toughness properties¹ of bone develop from this multi-scaled, hierarchical structure [1-4], which spans from nanometer to macroscopic dimensions (Figure 1) [5, 6]; indeed, these mechanical properties are derived from very different length-scales. This is especially true with respect to resistance to fracture where a suite of physical toughening mechanisms are activated at varying length-scales. Specifically, bone derives its toughness and hence its ability to resist fracture from both intrinsic and extrinsic mechanisms

¹ Stiffness is related to the elastic modulus and defines the force required to produce corresponding elastic deformation. Strength, defined by the yield stress at the onset of permanent deformation or maximum strength at the peak load before fracture, is a measure of the force/unit area that the bone can withstand. The fracture toughness measures the resistance to fracture of a material.

1
2
3
4 (Figure 1).² Principally at sub-micron dimensions, bone is toughened intrinsically
5 by “plasticity” (or more correctly, inelasticity) mechanisms; these include the
6 molecular uncoiling of the tropocollagen molecules at the nanoscale [6], and at
7 slightly coarser scales the sliding of mineralized collagen fibrils [9, 10]. At the
8 length-scales of 10 to 100's μm , conversely, the primary toughening mechanisms
9 in bone are extrinsic. These mechanisms affect solely the growth of cracks; they
10 involve processes of crack-tip shielding, most notably in bone by crack deflection
11 and twisting and bridging of the crack by fibrils or intact regions of bone matrix
12 in the crack wake, processes that are motivated by the presence of microcracks.
13 A central feature for extrinsic toughening is the specific nature of the crack path
14 which is controlled by the direction of the applied forces and the nature of the
15 microstructure, in particular the hyper-mineralized interfaces of the osteons
16 (cement lines), which provide microstructurally ‘weak’, and hence preferred,
17 paths for cracking. Microcracks most often form at these cement lines and are
18 thus primarily aligned with the osteonal orientation, *i.e.*, along the long axis of
19 the bone, with a typical spacing of $\sim 10\text{-}100\text{s } \mu\text{m}$ [11-15]. Indeed, $\sim 99\%$ of all
20 microcracks in bone are aligned at an angle of less than 25° with respect to the
21 osteons [16]. It is because of the orientation dependence of the microcracking,
22 and as well as the crack arrest and deflection as the crack encounters the cement
23 lines [11, 17], that the fracture properties of bone are highly anisotropic, with the
24 toughness in the transverse orientation being far higher than in the longitudinal
25 orientations, *i.e.*, bone is easier to split than to break.
26
27
28
29
30
31
32
33
34
35
36
37
38
39
40
41
42
43
44
45
46
47
48
49
50

51
52 ² *Intrinsic* toughening mechanisms operate ahead of the crack tip to generate resistance to
53 microstructural damage. The most prominent mechanism is that of plastic deformation which
54 provides a means of blunting the crack tip through the formation of “plastic” zones. *Extrinsic*
55 toughening mechanisms, conversely, operate primarily in the wake of the crack tip to inhibit
56 cracking by “shielding” the crack from the applied driving force [6-8]. Whereas intrinsic
57 toughening mechanisms are effective in inhibiting both the initiation and growth of cracks,
58 extrinsic mechanisms, *e.g.*, crack bridging, are only effective in inhibiting crack growth [6].
59
60
61
62
63
64
65

1
2
3
4 Such mechanical properties can be adversely affected, however, by biological
5 factors, such as aging and disease, and through exposure to irradiation. The
6 latter can occur in medical procedures and during scientific study. Medically,
7 bone allografts, a commonly used bone replacement in the orthopedic
8 reconstruction of bone, are invariably sterilized with gamma radiation to
9 minimize the spread of disease [18]. The optimum dosage, however, is
10 somewhat controversial as too much irradiation can cause damage to the
11 collagen matrices [19-22]. Tissue banks typically use between 10 and 35 kGy [21]
12 although 70 kGy is needed in order to sterilize against radiation-resistant
13 viruses.³ For scientific studies, bone is commonly sterilized by exposure to
14 radiation prior to testing; additionally, experiments involving *in situ* mechanical
15 tests performed in conjunction with x-ray micro-tomography or diffraction can
16 lead to exposures approaching 1 MGy or more⁴ [24-28]. The problem here is that
17 scientific observations and measurements on bone exposed to such radiation
18 doses may negate the validity of the results as the structure and properties of the
19 bone is no longer reflective of the human condition.
20
21
22
23
24
25
26
27
28
29
30
31
32
33
34
35
36
37

38 Recent studies [23] have shown a higher than expected effect of prior
39 irradiation in degrading the mechanical properties of human bone. Specifically,
40 as little as 70 kGy of radiation resulted in the total suppression of all post-yield
41 deformation (*i.e.*, plasticity) and after 210 kGy of irradiation, the fracture
42 toughness was decreased by a factor of five. The decreases in strength, ductility
43 and toughness with irradiation were attributed to (i) changes in crack path (the
44 extrinsic effect), and (ii) a degradation of the collagen integrity from collagen
45
46
47
48
49
50
51
52

53
54 ³ A Gray (Gy) is a unit of adsorbed dosage of ionizing radiation, equivalent to absorbed energy
55 per unit mass (1 Gy = 1 J/kg).

56 ⁴ A 2 mm thick bone sample is typically irradiated with ~100 Gy/s during tomographic imaging
57 with successive scans taking up to several hours. The final dose received during these tests can
58 involve several MGy [23], and is far above what would be considered a 'safe' threshold for bone
59 tissue.
60
61
62
63
64
65

1
2
3
4 damage (the intrinsic effect). Specifically, UV Raman spectra, which are known
5 to correlate with protein conformation because of the amide moiety in cross-
6 linking and bonding [29], indicated large increases in the amide I peak height
7 with increased irradiation dose [23], although due to the semi-quantitative
8 nature of spectroscopic data, the absolute levels of the cross-link profile remain
9 unknown.

10
11 In this study, we further examine the effects of x-ray irradiation on the
12 mechanical properties of human cortical bone over a more complete spectrum of
13 irradiation exposures, with focus on the so-called “safe” threshold dosage for
14 bone allografts (~25-35 kGy). We utilize a wide spectrum of “structure and
15 property” characterization techniques explicitly to identify the magnitude of the
16 irradiation-induced degradation in the strength, (post-yield) ductility and
17 toughness of human cortical bone and to discern the mechanistic role of
18 irradiation in affecting the bone-matrix structure and properties over multiple
19 length-scales from nanoscale to macroscopic dimensions. Specifically, in
20 addition to nonlinear elastic fracture mechanics measurements of the
21 macroscopic bone toughness, coupled with *in situ* environmental scanning
22 electron microscopy (eSEM) and post-testing three-dimensional synchrotron x-
23 ray computed micro-tomography of the microscopic crack paths, we employ
24 small- and wide-angle x-ray scattering/diffraction (SAXS/WAXD) of *in situ*
25 uniaxial tensile tests to examine the effectiveness of fibrillar sliding as a
26 nanoscale deformation mechanism in bone (by measuring the strain partitioning
27 between the mineral and collagen phases), and use deep UV Raman and Fourier
28 Transform Infrared (FTIR) spectroscopies and a fluorometric assay to
29 characterize the damage to the collagen fibrils.
30
31
32
33
34
35
36
37
38
39
40
41
42
43
44
45
46
47
48
49
50
51
52
53
54
55
56
57
58
59
60
61
62
63
64
65

2. Experimental methods

2.1 Material

Bone test samples were taken from the midsection of a frozen human cadaveric femoral cortical bone (male, aged 48 years old). They were machined into 40 tension specimens for strength and ductility measurements (with *in situ* SAXS/WAXD) and 49 bend specimens for fracture toughness testing (with *in situ* eSEM). All samples were kept refrigerated in Hanks' Balanced Salt Solution (HBSS) prior to irradiation and/or testing.

For bend tests, the 49 samples were divided into seven groups based on irradiation exposure: one control group (unirradiated), one group irradiated at a low dose typical of radiation therapy (50 Gy), three groups irradiated at varying doses that are typical of doses received during sterilization (25, 35, 70 kGy, respectively), and two groups irradiated at the typical dose received during one to three x-ray tomography scans (210, 630 kGy). X-ray irradiation was performed at the Advanced Light Source (ALS) synchrotron facility at the Lawrence Berkeley National Laboratory on a super-bend source. The dose rate at the ALS at the energy level of 20 keV is 110 Gy/s [23]. During irradiation, all of the samples were kept hydrated by wrapping the sample in an HBSS-soaked paper towel.

The samples for each of the seven irradiation groups were further divided into two groups for mechanical testing, three samples were used for three-point bending tests and the remaining four were used for crack resistance-curve (R-curves) measurements;⁵ test methods were in general accordance with ASTM standards [30]. Bend samples were machined along the long axis of the bone into 10-mm long rectangular bars (thickness $B = 1.5\text{-}2.0$ mm, width $W = 3\text{-}4$ mm). A flaw was produced in the fracture specimens by

⁵ The crack resistance- or R-curve provides an assessment of the fracture toughness in the presence of subcritical crack growth. It involves measurements of the crack-driving force, *e.g.*, the stress intensity K , strain-energy release rate G or J -integral, as a function of crack extension (Δa). The value of the driving force at $\Delta a \rightarrow 0$ provides a measure of the crack-initiation toughness whereas the slope and/or the maximum value of the R-curve can be used to characterize the crack-growth toughness.

1
2
3
4 using a low-speed diamond saw to cut an initial notch, which was then sharpened by
5 repeatedly sliding a razor blade over it with continuous irrigation with 1- μ m diamond
6 slurry. These procedures produced single-edge-notch bend (SE(B)) samples for R-curve
7 measurements with a consistent micro-notch root radius of \sim 3-5 μ m. Using this
8 technique sharp stress concentrators with initial crack length of $a \approx$ 1.5 -2 mm ($a/W \approx$ 0.5)
9 were produced. The notch was positioned so that the nominal crack growth was
10 perpendicular to the long axis of the bone (transverse orientation). Prior to testing, all of
11 the notched samples were given a final polish in a 0.05 μ m diamond suspension. Both
12 the notched (for R-curve testing) and unnotched (for strength testing) samples were
13 soaked in ambient HBSS for \sim 24 hr prior to testing.
14
15
16
17
18
19
20
21
22
23

24 The 40 samples for the *in situ* tension tests were sectioned using a low-speed saw
25 into \sim 10 mm long rectangular bars ($B \sim$ 100-200 μ m, $W \sim$ 1 mm), again parallel to the
26 bone's long axis of the bone; the final thickness was achieved by polishing with 800-grit
27 paper. Samples were left to dry in air for roughly 24 hr before 60-grit silicon carbide
28 paper was affixed to the ends of the samples with cyanoacrylate glue to form frictional
29 surfaces to grip during testing. Each sample had four horizontal lines drawn on with
30 marker to act as guides for optical tracking of the tissue strain. The samples for the *in*
31 *situ* tension tests were divided into two groups: a control group (unirradiated) and a
32 high-dose irradiation group (70 kGy).
33
34
35
36
37
38
39
40
41
42
43
44
45

46 2.2 Strength, toughness and R-curve measurements

47

48 Unnotched three-point bend tests (loading span of 7.5 mm) were performed, at a
49 displacement rate of 10 μ m/s, to generate basic constitutive data for the bone samples as
50 a function of irradiation dosage. From the resulting stress *vs.* strain curves, values of the
51 ultimate bending stress and strain were determined at the point of maximum load, the
52 bending stiffness was calculated from the slope of the stress/strain curves, and the work-
53
54
55
56
57
58
59
60
61
62
63
64
65

1
2
3
4 of-fracture computed from the area under these curve divided by twice the cross-
5 sectional area of the fracture surface.
6
7

8
9 In order to capture the contributions from both intrinsic (plasticity) and extrinsic
10 (shielding) toughening mechanisms acting in the bone, fracture toughness
11 measurements were performed using nonlinear-elastic fracture mechanics methods,
12 specifically involving the J -integral⁶; in contrast to linear-elastic methods, *e.g.*, using the
13 stress intensity K , these methods provide a more realistic description of the contribution
14 to the toughness from the energy consumed in plastic deformation⁷ prior to, and during,
15 fracture [11, 31, 32]. $J_R(\Delta a)$ R-curves were performed on hydrated bone in mode I
16 (tensile-opening) using SE(B) specimens with a crack-growth direction transverse to the
17 long axis of the osteons (transverse orientation). R-curves were measured with the
18 HBSS-saturated specimens *in situ* in a Hitachi S-4300SE/N eSEM (Hitachi America,
19 Pleasanton, CA) using a Gatan Microtest 2-kN bending stage (Gatan, Abington, UK).
20 Crack extension was monitored directly in back-scattered electron mode at a pressure of
21 35 Pa and a 25 kV excitation voltage. The test method involved three-point bending
22 with a loading span of 6 mm, with procedures conforming to ASTM Standard E1820-08
23 [30]. R-curve tests were terminated after approximately 700 μm of crack extension, such
24 that measured R-curve data were limited to small-scale bridging conditions, where the
25 size of the zone of crack bridges behind the crack tip remained small compared to the in-
26 plane test specimen dimensions. Samples that had not failed at this stage were stored
27 for subsequent tomography analysis.
28
29
30
31
32
33
34
35
36
37
38
39
40
41
42
43
44
45

46
47 Although nonlinear elastic J -integral measurements were made to define the driving
48 force for crack initiation and growth, data are presented in terms of the more familiar
49
50

51
52 ⁶ J is the nonlinear strain-energy release rate, *i.e.*, the rate of change in potential energy for a unit
53 increase in crack area in a nonlinear elastic solid. It is the nonlinear-elastic equivalent of the
54 strain-energy release rate G . It characterizes the stress and displacement fields at a crack tip in
55 such a solid, and as such can be used to define the onset of fracture there.
56

57 ⁷ Plastic deformation here is used as a general term to indicate any of the inelastic, non-
58 recoverable deformation mechanisms, such as local collagen fibrillar shearing, viscoplasticity,
59 and microcracking, that are active at various length-scales in bone [5, 6].
60
61
62
63
64
65

1
2
3
4 stress-intensity factor K using the following procedures. The equivalent K value at each
5 measured crack length was computed from the measured J values, which were
6 determined from the applied load and instantaneous crack length according to ASTM
7 standards [30]. Specifically, the J value was decomposed into its elastic and plastic
8 contributions:
9

$$10 \quad J = J_{el} + J_{pl}. \quad (1)$$

11 The elastic contribution J_{el} was determined from linear-elastic fracture mechanics:
12

$$13 \quad J_{el} = \frac{K_I^2}{E}, \quad (2)$$

14 where K_I is the mode I stress-intensity factor, and E is Young's modulus. Using the load-
15 line displacements, the plastic component J_{pl} for a stationary crack in bending is given
16 by:
17

$$18 \quad J_{pl} = \frac{1.9A_{pl}}{Bb}, \quad (3)$$

19 where A_{pl} is the plastic area under force *vs.* displacement curve, b is the uncracked
20 ligament length ($W-a$). K -based fracture toughness K_{Jc} values were then back-calculated
21 from the J measurements using the standard J - K equivalence for nominally mode I
22 fracture, specifically that $K_{Jc} = (J_c E)^{1/2}$.
23

24 Values of the Young's modulus E for the unirradiated and irradiated (70 kGy)
25 cortical bone were determined using nano-indentation. A total of 11 indentations were
26 performed using a Triboindenter (Hysitron, Inc.). At each location the reduced
27 modulus, (indicating the elastic properties of the bone extracellular matrix), was
28 determined. The results showed a true elastic modulus of 17 ± 5 GPa with no statistically
29 significant changes between the unirradiated and irradiated groups.
30

31 For all fracture toughness tests conducted, conditions for J -dominance, as specified
32 by the active ASTM standard [30], were met, *i.e.*, $b, B \gg 10 (J_c/\sigma_y)$, where σ_y is the flow
33 stress. This latter criterion ensures that the critical J_c (and calculated K_{Jc}) values
34 represent valid fracture toughness values.
35
36
37
38
39
40
41
42
43
44
45
46
47
48
49
50
51
52
53
54
55
56
57
58
59
60
61
62
63
64
65

2.3 Microstructural characterization

In addition to characterizing the bone-matrix microstructure and crack trajectories *in situ* with scanning electron microscopy (back-scattered electron mode) in the Hitachi S-4300SE/N eSEM, synchrotron x-ray computed micro-tomography (μ XCT) was employed to visualize the crack path and distribution of micro-damage in three-dimensions (after R-curve testing). The μ XCT evaluation was performed at the Advanced Light Source synchrotron radiation facility (Lawrence Berkeley National Laboratory, Berkeley, USA) with a setup similar to standard tomography procedures [33] in that samples are rotated in a monochromatic x-ray beam and the transmitted x-rays are imaged via a scintillator, magnifying lens and a digital camera to give an effective voxel size in the reconstructed three-dimensional image of 1.8 μ m. Hydrated samples were scanned in absorption mode and the reconstructed images were obtained using a filtered back-projection algorithm. In absorption mode, the gray scale values of the reconstructed image are representative of the absorption coefficient. To maximize the signal-to-noise ratio, 20 keV energy was selected to optimize the interaction between the x-rays and the sample. Two-dimensional images were taken every quarter of a degree between 0 and 180 degrees. The data sets were then reconstructed using the software Octopus [34] and the three-dimensional visualization was performed using AvizoTM software [35].

2.4 Synchrotron x-ray scattering and diffraction measurements (partitioning of strain)

Strength and ductility measurements were also made using uniaxial tension tests under conditions where simultaneous small-angle x-ray scattering (SAXS) and wide angle x-ray diffraction (WAXD) patterns could be taken in real time. For a given strain on the bone tissue, this enabled estimates of the individual strain carried by the collagen and mineral phases. Samples were mounted in a load frame at the Advanced Light Source synchrotron facility (Lawrence Berkeley National Laboratory, Berkeley, CA) so that the long axis of the bone was oriented perpendicular to the 10 keV x-rays; a schematic of the experimental setup is shown in [Figure 2](#). A tensile load was applied parallel to the long axis of the femur. The sample was kept hydrated 12 hr prior to the

1
2
3
4 experiment as well as throughout the experiment by means of a hydration cell
5 comprised of a strip of cellophane held to the sample through capillary action with a few
6 drops of HBSS.
7
8
9

10 A parallel beam of monochromatic x-rays (at an energy of 10 keV and a wavelength
11 of 0.124 nm) with a 1 mm x 0.25 mm cross-section was directed perpendicular to the
12 applied load. A high speed Pilatus detector was used for collecting SAXS data and a
13 Quantum CCD X-ray detector (Area Detector Systems Corporation) was used for
14 reading WAXD patterns. The sample was mounted into a custom built tensile stage
15 fitted with a 5-kgf load cell (Omega, LC703-10) and a motor-driven displacement stage.
16 All samples were loaded under displacement control at a displacement rate of 1 $\mu\text{m/s}$,
17 with SAXS/WAXD measurements taken at various points along the stress/strain curves,
18 with an exposure time for the frames of 0.5 s. The number of exposures was regulated in
19 order to keep the radiation dose below 30 kGy so that there would not be any additional
20 damage to the tissue due to the radiation received during *in situ* tensile testing;
21 specifically, the x-ray irradiation was blocked between exposures.
22
23
24
25
26
27
28
29
30
31
32
33

34 Synchrotron radiation was used to measure the SAXS and WAXD patterns which
35 were analyzed to find percent changes in the fibril and mineral strain along the tensile
36 axis. For the SAXS region of reciprocal space, the meridional collagen molecules in the
37 fibril have a staggered spacing of ~ 67 nm (this leads to a diffraction peak at a q-value
38 of $\sim 0.009 \text{ \AA}^{-1}$), where the mineral is primarily deposited between the heads and tails of
39 the collagen, leading to a diffraction pattern. The SAXS detector was located at a
40 distance of ~ 4100 mm from the sample in order to detect changes to the collagen peak
41 position. The WAXD detector was placed ~ 250 mm away from the sample. For the
42 WAXD region of reciprocal space the detector must be oriented to get diffraction from
43 the (0002) peak at a lattice spacing of ~ 0.344 nm. The sample-detector distance and the
44 beam center were both calibrated for the SAXS/WAXD data analysis using a silver
45 behenate standard. The analysis software IGORPro (Wavemetrics) and the custom
46 macro NIKA were then used in conjunction to convert the 2-D data to 1-D by radially
47 integrating the 2-D SAXS and WAXD patterns over azimuthal sectors. For this
48
49
50
51
52
53
54
55
56
57
58
59
60
61
62
63
64
65

1
2
3
4 experiment SAXS/WAXD patterns were integrated in a narrow pie shaped sector with a
5
6 10° angular width that was centered along the tensile axis. After integration the peaks
7
8 representing the first order reflection from the meridional collagen SAXS pattern and
9
10 around the (0002) reflection from the apatite WAXD pattern were fit using a Gaussian
11
12 function and a fourth order polynomial. The peak positions were used to find,
13
14 respectively, the collagen fibril *D*-spacing and the (0002) crystallographic lattice spacing
15
16 relative to the unstressed state (defined at zero load for each sample).
17

18 The tissue strain was measured by measuring percent changes in the distance
19
20 between the two horizontal lines on either end of the samples using image analysis
21
22 software (National Instruments Vision Assistant 8.5). This was achieved using a CCD
23
24 camera synchronized with the detectors to take images when the samples were exposed
25
26 to x-rays during testing.
27

28 29 *2.5 Fourier transform infrared spectroscopy*

30
31 Fourier transform infrared (FTIR) spectroscopy was used in transmission mode
32
33 to assess the degree of enzymatic cross-linking in the collagen for two groups: healthy
34
35 (unirradiated) and irradiated (70 kGy) human cortical bone. Ten samples of human
36
37 cortical bone were sectioned with a low-speed saw. The tissue was dehydrated with a
38
39 series of ethanol baths to remove the water component, which has a strong absorbance
40
41 in the IR spectrum. The samples were then embedded in Technovit 7100 (Kultzer & Co,
42
43 Wehrheim, Germany), a liquid containing hydroxyethyl-methacrylate, according to the
44
45 manufacturer's instructions. Briefly, Technovit 7100 was admixed with hardener I and II
46
47 at 300:3:20 v/w/v ratio, as described in [36]. The embedded tissue was then sectioned
48
49 with a microtome to a final dimension of $\sim 1 \text{ mm} \times 1 \text{ mm} \times 2 \text{ }\mu\text{m}$ as a 1-5 μm thickness is
50
51 required to analyze the samples with IR beam in transmission.
52

53 The protein Amide I (peptide bond C=O stretch) undergoes frequency and intensity
54
55 changes as a result of changes in protein secondary structure [37]. One of the unique
56
57 capabilities of FTIR spectroscopy is the ability to quantify these changes, specifically by
58
59 tracking the spatial variation of the collagen components in mineralized tissue.
60
61
62
63
64
65

1
2
3
4 Information on the protein structure can be extracted from broad spectral bands
5 consisting of components of peaks resulting from Amide I modes of various secondary
6 structures by using a spectral resolution technique [38]. For type I collagen in bone the
7 two major components of importance are the enzymatic collagen cross-links:
8 pyridinoline (Pyr) and divalent dehydrodihydroxynorleucine (DHLNL). Indeed, the
9 ratio of peak areas of the Pyr and DHLNL subbands, at 1660 cm^{-1} and 1690 cm^{-1}
10 respectively, provides a semi-quantitative measure of the cross-linking profile in the
11 collagen matrix; this ratio has been correlated to the relative amounts of enzymatic
12 cross-links, specifically mature non-reducible (interfibrillar) cross-links and immature
13 reducible (intrafibrillar) cross-links (Figure 1). A method has been developed to enable
14 spectral analysis of the amide I band to isolate peaks corresponding to these two major
15 type I collagen cross-links, namely pyridinoline (pyr) and DHLNL, [39] using second-
16 derivative spectroscopy. All FTIR spectroscopy data were obtained using a
17 conventional Globar IR source at the Advanced Light Source (Lawrence Berkeley
18 National Laboratory, Berkeley, USA). Image spectroscopy consists of a source, a sample
19 handling unit and a focal plane array detector on an IR microscope. The instrument is
20 equipped with a photographic device to capture an image of the area of the tissue being
21 examined. The recorded spectra were taken in transmission mode with 128 scans and
22 had a spectral resolution of 4 cm^{-1} and a spot size of $\sim 150 \mu\text{m}$. OMNIC software (Thermo
23 Fischer) was used for data processing.

24 25 26 27 28 29 30 31 32 33 34 35 36 37 38 39 40 41 42 43 44 45 46 47 48 49 50 51 52 53 54 55 56 57 58 59 60 61 62 63 64 65

2.6 Deep ultraviolet Raman spectroscopy

The collagen cross-linking profile was further characterized using deep-ultraviolet Raman spectroscopy, with a 244-nm excitation source [23]. The UV Raman technique eliminates the fluorescence interference found with visible excitation. Also, due to resonance effects, the signal strength of some features from the organic phase (particularly those associated with the amide moiety formed by the bonds between peptides) are enhanced relative to those from the inorganic phase (*e.g.*, phosphate and carbonate stretching modes). To avoid damage to the sample the laser power was kept

1
2
3
4 below 5 mW and the sample was rotated at ~45 rpm. It is known [23, 29] that the height
5 of the amide I feature at 1650 cm^{-1} is sensitive to the collagen environment, in particular
6 to the extent of cross-linking, increasing, for example, with dehydration or with
7 increasing tissue age. For quantitative analysis of this effect, spectra were processed by
8 subtracting a small linear background defined by the signal at 500 and 2000 cm^{-1} and
9 then normalizing to the height of the CH_2 wag peak at 1460 cm^{-1} (this peak does not have
10 a strong resonance enhancement).
11
12
13
14
15
16
17

18 *2.7 Accumulation of advanced glycation end-products*

19
20
21 Bone collagen is also susceptible to the age-related accumulation of non-enzymatic
22 cross-links resulting from the covalent bonding of oxidizing sugars and free amino
23 groups on the collagen protein including arginine and lysine. These cross-links are
24 known as advanced glycation end-products (AGEs) and they form both intra- and inter-
25 fibrillar links along the collagen backbone [40]. The AGEs were quantified using a
26 fluorometric assay on both unirradiated bone and bone irradiated at 70 kGy. For each
27 sample a section of the femoral midshaft was demineralized using
28 ethylenediaminetetraacetic acid (EDTA) and then hydrolyzed using 6N HCl for 24 hr at
29 110°C . AGE content was determined using fluorescence readings taken using a
30 microplate reader at the excitation wavelength of 370 nm and emission wavelength of
31 440 nm. These readings were standardized to a quinine-sulfate standard and then
32 normalized to the amount of collagen present in each bone sample. The amount of
33 collagen for each sample was determined based on the amount of hydroxyproline, the
34 latter being determined using a chloramine-T colorimetric assay that recorded the
35 absorbance of the hydrolysates against a commercially available hydroxyproline
36 standard at the wavelength of 585 nm [41].
37
38
39
40
41
42
43
44
45
46
47
48
49
50
51
52
53
54
55

56 **3. Results**

57 *3.1 Strength, ductility and fracture toughness*

1
2
3
4 Bending stress-strain curves, which assess the macroscopic strength and
5 ductility, and fracture toughness R-curves of human cortical bone irradiated at
6 varying degrees of x-ray irradiation (0, 0.05, 25, 35, 70, 210, 630 kGy), are shown
7 in **Figure 3**. Data show that for irradiation exposures starting between 35-70
8 kGy, there is a severe dose-dependent degradation in mechanical properties; no
9 effect could be discerned at 35 kGy and below. Above this level though, there
10 was a complete loss in post-yield deformation (plasticity) coupled with a
11 progressive and very severe reduction in the ultimate (maximum) bending
12 strength, bending strain and toughness, although little change was seen in the
13 bending stiffness. Specifically, compared to unirradiated bone, exposures of 70,
14 210 and 630 kGy resulted in a respective decrease in the strength of the bone by
15 ~25%, 60% and more than 80%, while a similar trend was observed for the
16 ultimate strain (Fig. 3a), consistent with previous studies that showed that γ - and
17 x-irradiation can degrade the plastic, rather than elastic, properties of bone, such
18 as bending strength and toughness [22, 42-47].

19
20
21
22
23
24
25
26
27
28
29
30
31
32
33
34
35
36
37 The corresponding toughness properties, in terms of full $K_R(\Delta a)$ R-curves for
38 physiologically relevant small cracks ($\Delta a < 700 \mu\text{m}$), are plotted in Fig. 3b for all
39 seven irradiation groups. It was observed that even though the stress-strain
40 curves showed a severe loss in the plastic properties of bone with high doses of
41 irradiation, rising R-curve behavior is still exhibited (albeit diminished), even
42 after all plasticity is lost, indicating that some limited degree of extrinsic
43 toughening, *e.g.*, from crack deflection and/or crack bridging, is still active.
44
45
46
47
48
49
50
51
52
53
54
55
56
57
58
59
60
61
62
63
64
65
66
67
68
69
70
71
72
73
74
75
76
77
78
79
80
81
82
83
84
85
86
87
88
89
90
91
92
93
94
95
96
97
98
99
100
101
102
103
104
105
106
107
108
109
110
111
112
113
114
115
116
117
118
119
120
121
122
123
124
125
126
127
128
129
130
131
132
133
134
135
136
137
138
139
140
141
142
143
144
145
146
147
148
149
150
151
152
153
154
155
156
157
158
159
160
161
162
163
164
165
166
167
168
169
170
171
172
173
174
175
176
177
178
179
180
181
182
183
184
185
186
187
188
189
190
191
192
193
194
195
196
197
198
199
200
201
202
203
204
205
206
207
208
209
210
211
212
213
214
215
216
217
218
219
220
221
222
223
224
225
226
227
228
229
230
231
232
233
234
235
236
237
238
239
240
241
242
243
244
245
246
247
248
249
250
251
252
253
254
255
256
257
258
259
260
261
262
263
264
265
266
267
268
269
270
271
272
273
274
275
276
277
278
279
280
281
282
283
284
285
286
287
288
289
290
291
292
293
294
295
296
297
298
299
300
301
302
303
304
305
306
307
308
309
310
311
312
313
314
315
316
317
318
319
320
321
322
323
324
325
326
327
328
329
330
331
332
333
334
335
336
337
338
339
340
341
342
343
344
345
346
347
348
349
350
351
352
353
354
355
356
357
358
359
360
361
362
363
364
365
366
367
368
369
370
371
372
373
374
375
376
377
378
379
380
381
382
383
384
385
386
387
388
389
390
391
392
393
394
395
396
397
398
399
400
401
402
403
404
405
406
407
408
409
410
411
412
413
414
415
416
417
418
419
420
421
422
423
424
425
426
427
428
429
430
431
432
433
434
435
436
437
438
439
440
441
442
443
444
445
446
447
448
449
450
451
452
453
454
455
456
457
458
459
460
461
462
463
464
465
466
467
468
469
470
471
472
473
474
475
476
477
478
479
480
481
482
483
484
485
486
487
488
489
490
491
492
493
494
495
496
497
498
499
500
501
502
503
504
505
506
507
508
509
510
511
512
513
514
515
516
517
518
519
520
521
522
523
524
525
526
527
528
529
530
531
532
533
534
535
536
537
538
539
540
541
542
543
544
545
546
547
548
549
550
551
552
553
554
555
556
557
558
559
560
561
562
563
564
565
566
567
568
569
570
571
572
573
574
575
576
577
578
579
580
581
582
583
584
585
586
587
588
589
590
591
592
593
594
595
596
597
598
599
600
601
602
603
604
605
606
607
608
609
610
611
612
613
614
615
616
617
618
619
620
621
622
623
624
625
626
627
628
629
630
631
632
633
634
635
636
637
638
639
640
641
642
643
644
645
646
647
648
649
650
651
652
653
654
655
656
657
658
659
660
661
662
663
664
665
666
667
668
669
670
671
672
673
674
675
676
677
678
679
680
681
682
683
684
685
686
687
688
689
690
691
692
693
694
695
696
697
698
699
700
701
702
703
704
705
706
707
708
709
710
711
712
713
714
715
716
717
718
719
720
721
722
723
724
725
726
727
728
729
730
731
732
733
734
735
736
737
738
739
740
741
742
743
744
745
746
747
748
749
750
751
752
753
754
755
756
757
758
759
760
761
762
763
764
765
766
767
768
769
770
771
772
773
774
775
776
777
778
779
780
781
782
783
784
785
786
787
788
789
790
791
792
793
794
795
796
797
798
799
800
801
802
803
804
805
806
807
808
809
810
811
812
813
814
815
816
817
818
819
820
821
822
823
824
825
826
827
828
829
830
831
832
833
834
835
836
837
838
839
840
841
842
843
844
845
846
847
848
849
850
851
852
853
854
855
856
857
858
859
860
861
862
863
864
865
866
867
868
869
870
871
872
873
874
875
876
877
878
879
880
881
882
883
884
885
886
887
888
889
890
891
892
893
894
895
896
897
898
899
900
901
902
903
904
905
906
907
908
909
910
911
912
913
914
915
916
917
918
919
920
921
922
923
924
925
926
927
928
929
930
931
932
933
934
935
936
937
938
939
940
941
942
943
944
945
946
947
948
949
950
951
952
953
954
955
956
957
958
959
960
961
962
963
964
965
966
967
968
969
970
971
972
973
974
975
976
977
978
979
980
981
982
983
984
985
986
987
988
989
990
991
992
993
994
995
996
997
998
999
1000

1
2
3
4 factor of five lower after 210 kGy irradiation, *i.e.*, from values of 13.3 MPa $\sqrt{\text{m}}$ ($J_c \sim$
5 9 kJ/m 2) in unirradiated samples down to 2.7 MPa $\sqrt{\text{m}}$ ($J_c \sim 0.3$ kJ/m 2) in the 210
6
7 kGy irradiated samples; similarly, K_{Jc} values were 10.5 MPa $\sqrt{\text{m}}$ ($J_c \sim 5$ kJ/m 2) and
8
9 7.4 MPa $\sqrt{\text{m}}$ ($J_c \sim 3$ kJ/m 2), respectively, after 50 Gy and 70 kGy of radiation.
10
11
12
13

14 *3.2 Crack path observations*

15
16 The nature of the crack trajectories in relation to the microstructure is
17 illustrated in **Figure 4** for human cortical bone subjected to (a-c) low dose (50 Gy)
18 and (e-f) high dose (\sim MGy) x-ray irradiation as two-dimensional x-ray
19 tomographic images (a,c) and (d,f) and three-dimensional representations (b) and
20 (e) of the crack path and Haversian canals. Specifically, Figs. 4a,b,c show how
21 the growing crack is severely deflected and twisted as it encounters the osteons
22 in low dose irradiated bone, with the result that the crack path is highly deflected
23 in all orientations. Such characteristic features of extrinsic toughening are typical
24 of unirradiated bone [11, 48], and are consistent with the notion that irradiation
25 exposures of 50 Gy do not appear to significantly harm the toughness properties
26 of the bone. In stark contrast, the crack trajectories in the severely irradiated
27 bone, shown in Figs. 4d,e,f, are quite different, with far less evidence of major
28 crack deflections at the osteon boundaries and a resulting relatively planar crack
29 path. The mechanisms of crack deflection and twist are still operative, but their
30 limited size leads to much smaller amplitude deviations in crack path and hence
31 to lower toughness, consistent with the macroscale test data in Fig. 3.
32
33
34
35
36
37
38
39
40
41
42
43
44
45
46
47
48
49
50

51 *3.2 SAXS/WAXD for tissue strain measurements*

52
53 To further investigate the loss in plasticity with irradiation, hydrated bone
54 samples were loaded in uniaxial tension with simultaneous examination using
55 SAXS/WAXD. For a given strain in the bone tissue sample, the individual
56
57
58
59
60
61
62
63
64
65

1
2
3
4 strains in the collagen and mineral were measured in human cortical bone
5 exposed to 70 kGy of x-ray irradiation, as compared to unirradiated bone.
6
7 Results are shown in Figs. 5a,b, respectively, for the variation in individual
8 strains in the collagen fibrils (ϵ_F) and in the mineral (ϵ_M), as a function of the
9 global strain (ϵ_T) applied to the bone tissue. With increasing tissue strain, a linear
10 increase in both the fibrillar and mineral strain is apparent, until yielding occurs
11 at roughly 1% tissue strain (Fig. 6); at this point most of the strain continues to be
12 carried by the collagen, but not in the irradiated bone, which then fractures.
13 With plastic deformation, the fibrillar and mineral strains assume approximately
14 constant values (~1.1% in the collagen, ~0.2% in the mineral), consistent with
15 results in the literature [10]. Following 70 kGy irradiation, however, the fibrillar
16 strains are roughly up to 50% lower for a given tissue strain, and the sample fails
17 catastrophically with little to no evidence of post-yield deformation, indicative of
18 the loss of plasticity in highly irradiated bone. The actual ratios of fibrillar to
19 tissue strain (ϵ_F/ϵ_T) and mineral to tissue strain (ϵ_M/ϵ_T) are plotted for both groups
20 in Fig. 6 to compensate for sample-to-sample variability. The strain carried by
21 the collagen fibrils in the 70 kGy irradiated samples is ~40% of the applied tissue
22 strain, which is considerably lower than in the unirradiated bone where the fibril
23 strain is ~80% of the tissue strain. The effect is summarized in Figure 7 where at
24 an applied tissue strain of 0.85%, exposure to 70 kGy of irradiation causes a ~40%
25 decrease in the strain carried by the collagen fibrils and a ~20% decrease in
26 mineral strain, as compared to unirradiated bone. The data for the tissue and
27 mineral strain are both binned in regular intervals of tissue strain ($N=20$ for each
28 group), with error bars representing the standard errors of mean.

3.3 Quantification of collagen cross-linking

1
2
3
4
5
6
7
8
9
10
11
12
13
14
15
16
17
18
19
20
21
22
23
24
25
26
27
28
29
30
31
32
33
34
35
36
37
38
39
40
41
42
43
44
45
46
47
48
49
50
51
52
53
54
55
56
57
58
59
60
61
62
63
64
65

As high doses of irradiation are known to impart severe damage to the collagen matrix in the form of breaking of peptide bonds in the collagen backbone [21, 23, 49], the nature of the collagen environments was examined specifically using a number of techniques.

As we reported previously [23], results from deep UV-Raman spectra, shown in **Figure 8** for (hydrated) unirradiated and all irradiated groups of bone, indicate a very pronounced increase in the amide I peak after exposure to x-rays, implying severe damage of the collagen with increasing degree of irradiation. Although this indicates significant changes in the collagen environment associated with increased cross-linking, the identification of the specific nature of the cross-links with this technique remains uncertain.

For this reason, in the present study we performed additional Fourier transform infrared (FTIR) spectroscopy on unirradiated and 70 kGy irradiated bone. The protein amide I (peptide bond C=O stretch) mode near 1650 cm^{-1} undergoes frequency and intensity changes as a result of changes in protein secondary structure. FTIR spectroscopy gives quantitative information on the collagen maturity in bone, specifically the ratio of two of the major enzymatic collagen cross-links: specifically, the mature (non-reducible) divalent cross-links (Pyr) and the enzymatic immature (reducible) divalent dehydrodihydroxynorleucine cross-links (deH-DHLNL). Of these components the relative percent area ratio of the two sub-bands at $\sim 1660 \text{ cm}^{-1}$ and $\sim 1690 \text{ cm}^{-1}$ is related to collagen cross links that are abundant in mineralized tissue (Pyr and deH-DHLNL, respectively) [39]. For our results (**Figure 9**), a comparison of the calculated 1660:1690 spectroscopic ratio of these two peaks in the two groups of bone is shown in Fig. 9a. The ratios are calculated using second derivative spectroscopy which locates the position of the underlying bands within the amide I region and then peak fits these sub-bands to obtain information on the

1
2
3
4 relative percent area contribution of each underlying component for the
5 unirradiated and 70 kGy irradiated groups. The 1660:1690 peak area ratio
6 appears to correspond to the ratio of non-reducible (mature) to reducible
7 (immature) collagen cross-links in bone [39]. The results show that following 70
8 kGy irradiation, the 1660:1690 ratio decreases by almost two-thirds, indicating
9 that the damaging effects of irradiation affect the mature cross-links such as Pyr
10 to a greater degree than the immature cross-links such as deH-DHLNL.
11
12
13
14
15
16
17
18

19 The quantification of non-enzymatic cross-links was achieved via a
20 fluorometric assay that determines the relative intrinsic fluorescence due to
21 advanced glycation end-products (AGEs) relative to the amount of collagen in
22 the bone matrix. We find that bone which has been exposed to 70 kGy
23 irradiation has an elevated concentration of AGEs, on the order of ~21%, as
24 compared to that in unirradiated bone (Figure 10).
25
26
27
28
29
30
31

32 33 **4. Discussion**

34
35 Although irradiation is known to deleteriously degrade the structure and
36 mechanical properties of bone, we show in this work that the effect can be
37 extremely severe; indeed, the tissue can be dramatically and irreversibly
38 embrittled with major losses in strength, ductility and fracture resistance
39 following exposures in excess of 35 kGy. Specifically, compared to healthy
40 (unirradiated) human cortical bone, we find that bone strengths are reduced by
41 ~60% and more than 80% for irradiation doses of 210 and 630 kGy, respectively,
42 with a factor of five loss in fracture toughness at 210 kGy. Additionally, for x-ray
43 irradiation exposures above ~70 kGy, the bone no longer displays evidence of
44 post-yield (“plastic”) deformation, simply failing at its elastic limit (Fig. 3).
45
46
47
48
49
50
51
52
53
54
55
56

57 We explain these effects in terms of how the irradiation affects the intrinsic
58 and extrinsic contributions to the bone toughness, which are developed at widely
59
60
61
62
63
64
65

1
2
3
4 different structural length-scales. At micro- to macro-scales, the major
5 contributions to the fracture toughness originate extrinsically through such
6 mechanisms as crack deflection and bridging. The key here is the occurrence of
7 microcracking, which predominates along the “weaker” hyper-mineralized
8 interfaces of the osteons (cement lines) and to a lesser extent along the lamellar
9 boundaries. In the longitudinal orientations, (cement line) microcracks are
10 aligned roughly parallel to the growing crack; their formation alongside and
11 ahead of the crack tip leaves locally intact regions that can act as bridges across
12 the crack (“uncracked-ligament” bridging), and can carry load that would
13 otherwise be used to promote cracking [48]. The extent of toughening, however,
14 is far larger in the transverse direction, the orientation examined in this study, as
15 the microcracks are now aligned roughly perpendicular to the crack path where
16 they act as “delamination barriers” [11, 17]; this serves to locally arrest growing
17 cracks, cause marked crack deflections and crack twists, generate highly tortuous
18 crack paths, extremely rough fracture surfaces, and correspondingly high
19 toughness (Figs. 4a,b,c). Specifically, the growing cracks deflect by as much as 90
20 degrees as they encounter these interfaces between the interstitial bone and the
21 osteons; the consequent marked crack deflections and through-thickness twists
22 (Figs. 4a,b,c) are the primary source of (extrinsic) toughening in the transverse
23 orientation.

24
25
26
27
28
29
30
31
32
33
34
35
36
37
38
39
40
41
42
43
44
45
46
47 Prior exposure to x-rays at dosages in excess of ~70 kGy, however, leads to
48 radical changes in the crack path (Figs. 4d,e,f). Although growing cracks are still
49 subject to such microstructurally-induced deflections, the deflections are far
50 smaller in magnitude (although more frequent) resulting in minimal crack-path
51 deviations and an essentially linear crack trajectory (Figs. 4d,e,f). It is the
52 absence of such highly tortuous crack paths in irradiation-damaged bone, with
53 minimal deviations from the plane of maximum tensile stress, that serves to
54
55
56
57
58
59
60
61
62
63
64
65

1
2
3
4 curtail the high extrinsic toughness which is characteristic of healthy bone in the
5
6 transverse orientation.
7

8
9 In many respects though, it is the effects of irradiation on the intrinsic
10 contributions to the bone toughness that are more interesting. These
11 contributions arise at much smaller (sub-micron) length-scales and are associated
12 primarily with the generation of “plasticity” in bone from the process of fibrillar
13 sliding, which can occur at both the fibril [10] and fiber [50] level. Within the
14 fibrils non-recoverable deformation mechanisms take place, such as sliding at the
15 HA/tropocollagen interface [9], increased intermolecular cross-linking density
16 [40] and sacrificial bonding [51]; these mechanisms constrain molecular
17 stretching and provide the basis for the increased apparent strength of the
18 collagen molecules without catastrophic failure of either of the individual
19 components. The molecular behavior of the protein and mineral phases (fibrillar
20 sliding) within a fibril enables a large amount of dissipative deformation energy
21 once plastic yielding begins in mineralized tissues [10, 52, 53] and other
22 biological materials [54]. At the nano-scale the predominant plasticity
23 mechanisms are represented by this model of load transfer. As is common in
24 most materials, plasticity contributes to the intrinsic toughness by dissipating
25 energy and forming “plastic zones” surrounding crack-like defects that further
26 serve to blunt crack tips, thereby protecting the integrity of the entire structure
27 by reducing the driving force (*i.e.*, stress intensity) for crack propagation.
28
29

30
31 Changes to the effectiveness of this intrinsic mechanism are largely
32 influenced by the organic matrix. In this regard, damage to the collagen matrix
33 induced by irradiation can be extremely problematic to the biomechanical
34 properties of bone, in particular through the formation of collagen cross-links
35 [55-58] and eventually breakage of the backbone of the collagen molecule. In this
36 regard, the profile and distribution of collagen cross-links have a major influence
37
38
39
40
41
42
43
44
45
46
47
48
49
50
51
52
53
54
55
56
57
58
59
60
61
62
63
64
65

1
2
3
4 on bone function. As noted, three major types of collagen cross-links are found
5 in human cortical bone: enzymatic immature (reducible) divalent cross-links
6 (dehydrodi-hydroxynorleucine) and mature (non-reducible) divalent
7 (pyridinoline and pyrrole) cross-links linking neighboring fibrils, and the non-
8 enzymatic advanced glycation end-products (AGEs) that form both
9 intermolecular and interfibrillar cross-links along the collagen backbone.
10 Intermolecular cross-linking provides the fibrillar matrices with properties such
11 as tensile strength and viscoelasticity [40, 59-61]. The staggered array of type I
12 collagen, the primary type found in bone, relays strength in tension; the cross-
13 links keep the array in conformity - if there are too many cross-links collagens
14 ability to absorb energy declines, if there are too few the array may break apart.
15 A similar effect is thought to occur at the next structural level between arrays of
16 fibrils [50], which are linked via non-collagenous proteins and cross-linking.

17
18
19
20
21
22
23
24
25
26
27
28
29
30
31
32 In the current work, macroscopic mechanical tests clearly indicate that a
33 primary aspect of the irradiation-induced loss in fracture resistance can be
34 attributed to a complete loss in post-yielding (plastic) deformation (intrinsic
35 toughness) for radiation exposures of 70 kGy and above. Based on SAXS/WAXD
36 analyses and associated cross-link measurements, we interpret this in terms of a
37 suppression of the prevailing plasticity mechanism in bone of fibrillar sliding,
38 which results principally from a change in the proportion of the three types of
39 collagen cross-linking caused by the irradiation damage.

40
41
42
43
44
45
46
47
48
49
50
51
52
53
54
55
56
57
58
59
60
61
62
63
64
65
66
67
68
69
70
71
72
73
74
75
76
77
78
79
80
81
82
83
84
85
86
87
88
89
90
91
92
93
94
95
96
97
98
99
100
101
102
103
104
105
106
107
108
109
110
111
112
113
114
115
116
117
118
119
120
121
122
123
124
125
126
127
128
129
130
131
132
133
134
135
136
137
138
139
140
141
142
143
144
145
146
147
148
149
150
151
152
153
154
155
156
157
158
159
160
161
162
163
164
165
166
167
168
169
170
171
172
173
174
175
176
177
178
179
180
181
182
183
184
185
186
187
188
189
190
191
192
193
194
195
196
197
198
199
200
201
202
203
204
205
206
207
208
209
210
211
212
213
214
215
216
217
218
219
220
221
222
223
224
225
226
227
228
229
230
231
232
233
234
235
236
237
238
239
240
241
242
243
244
245
246
247
248
249
250
251
252
253
254
255
256
257
258
259
260
261
262
263
264
265
266
267
268
269
270
271
272
273
274
275
276
277
278
279
280
281
282
283
284
285
286
287
288
289
290
291
292
293
294
295
296
297
298
299
300
301
302
303
304
305
306
307
308
309
310
311
312
313
314
315
316
317
318
319
320
321
322
323
324
325
326
327
328
329
330
331
332
333
334
335
336
337
338
339
340
341
342
343
344
345
346
347
348
349
350
351
352
353
354
355
356
357
358
359
360
361
362
363
364
365
366
367
368
369
370
371
372
373
374
375
376
377
378
379
380
381
382
383
384
385
386
387
388
389
390
391
392
393
394
395
396
397
398
399
400
401
402
403
404
405
406
407
408
409
410
411
412
413
414
415
416
417
418
419
420
421
422
423
424
425
426
427
428
429
430
431
432
433
434
435
436
437
438
439
440
441
442
443
444
445
446
447
448
449
450
451
452
453
454
455
456
457
458
459
460
461
462
463
464
465
466
467
468
469
470
471
472
473
474
475
476
477
478
479
480
481
482
483
484
485
486
487
488
489
490
491
492
493
494
495
496
497
498
499
500
501
502
503
504
505
506
507
508
509
510
511
512
513
514
515
516
517
518
519
520
521
522
523
524
525
526
527
528
529
530
531
532
533
534
535
536
537
538
539
540
541
542
543
544
545
546
547
548
549
550
551
552
553
554
555
556
557
558
559
560
561
562
563
564
565
566
567
568
569
570
571
572
573
574
575
576
577
578
579
580
581
582
583
584
585
586
587
588
589
590
591
592
593
594
595
596
597
598
599
600
601
602
603
604
605
606
607
608
609
610
611
612
613
614
615
616
617
618
619
620
621
622
623
624
625
626
627
628
629
630
631
632
633
634
635
636
637
638
639
640
641
642
643
644
645
646
647
648
649
650
651
652
653
654
655
656
657
658
659
660
661
662
663
664
665
666
667
668
669
670
671
672
673
674
675
676
677
678
679
680
681
682
683
684
685
686
687
688
689
690
691
692
693
694
695
696
697
698
699
700
701
702
703
704
705
706
707
708
709
710
711
712
713
714
715
716
717
718
719
720
721
722
723
724
725
726
727
728
729
730
731
732
733
734
735
736
737
738
739
740
741
742
743
744
745
746
747
748
749
750
751
752
753
754
755
756
757
758
759
760
761
762
763
764
765
766
767
768
769
770
771
772
773
774
775
776
777
778
779
780
781
782
783
784
785
786
787
788
789
790
791
792
793
794
795
796
797
798
799
800
801
802
803
804
805
806
807
808
809
810
811
812
813
814
815
816
817
818
819
820
821
822
823
824
825
826
827
828
829
830
831
832
833
834
835
836
837
838
839
840
841
842
843
844
845
846
847
848
849
850
851
852
853
854
855
856
857
858
859
860
861
862
863
864
865
866
867
868
869
870
871
872
873
874
875
876
877
878
879
880
881
882
883
884
885
886
887
888
889
890
891
892
893
894
895
896
897
898
899
900
901
902
903
904
905
906
907
908
909
910
911
912
913
914
915
916
917
918
919
920
921
922
923
924
925
926
927
928
929
930
931
932
933
934
935
936
937
938
939
940
941
942
943
944
945
946
947
948
949
950
951
952
953
954
955
956
957
958
959
960
961
962
963
964
965
966
967
968
969
970
971
972
973
974
975
976
977
978
979
980
981
982
983
984
985
986
987
988
989
990
991
992
993
994
995
996
997
998
999
1000

At the onset of plastic deformation in healthy (unirradiated) bone (Figs. 5-6), the strain in the mineral becomes roughly constant with increasing tissue strain (Fig. 5b). Initially the load in the bone is carried by the mineral particles through shearing of the collagen matrix [62], but once yielding occurs the mineralized fibril and the fibril matrix begin to decouple [53]; a schematic interpretation for the load transfer in bone is shown in Figure 7. The tensile strain can be divided

1
2
3
4 into two contributions: first from the tensile stretching of the mineralized
5 collagen fibrils (which we studied by examining changes in the 67 nm D-spacing)
6 and second by shear deformation of the interfibrillar matrix and, at the smallest
7 length-scale, by shearing of the collagen matrix through the transfer of stress
8 between the stiff mineral platelets [10, 63]. In contrast, once plastic deformation
9 begins in the irradiated bone, the tissue fails due to degradation of the collagen
10 matrix, which acts to totally eliminate the bone's capacity for plastic deformation;
11 in materials science terms, the bone simply "embrittles" due to irradiation.
12
13
14
15
16
17
18
19
20

21 Our spectroscopy and fluorometric measurements (Figs. 8-10) strongly
22 suggest that this progressive irradiation-induced embrittlement of bone in the
23 form of the suppression of plasticity from fibrillar sliding and the consequent
24 major losses in toughness initially result from an increase in specific collagen
25 cross-linking which raises the amount of bonds; further irradiation exposures can
26 cause molecular damage due to breaking the peptide backbone. Irradiation
27 exposure leads to the release of free radicals via radiolysis of water molecules in
28 bone which can severely degrade the collagen molecules in addition to restricting
29 fibrillar sliding mechanisms [21, 49, 64].
30
31
32
33
34
35
36
37
38
39
40

41 Specifically, we observe a significant change in the magnitude of the amide I
42 peak in UV Raman spectra with radiation indicative of a radically changed
43 collagen environment (Fig. 8). Indeed, these measurements show that for a very
44 large exposure of 630 kGy, the spectral features were broadened to such an
45 extent that the individual peaks could not be observed, which is likely associated
46 with breaking of peptide bonds in the collagen backbone [49]. Although this
47 change in the height of the amide I peak has been related to collagen cross-
48 linking [23, 29], we obtained further information on the nature of these cross-
49 links using FTIR spectroscopy techniques to measure the vibrational energies of
50 molecules to detect changes to the structure of the collagen. Past studies [22, 65]
51
52
53
54
55
56
57
58
59
60
61
62
63
64
65

1
2
3
4 have used this procedure to examine the effects of gamma irradiation on the
5 mechanical and material properties of tendon, which is primarily comprised of
6 type I collagen organized in parallel arrays, and have reported changes to the
7 cross-linking in collagen with increased exposure to irradiation. The collagen in
8 both tendon and bone is stabilized by interfibrillar and intermolecular cross-
9 links, the primary mature cross-link is hydroxypyridinium; indeed, one study
10 demonstrated [22] a significant decreases in hydroxypyridinium cross-link
11 density with 60 kGy of irradiation. High doses of irradiation may also induce
12 changes in the material properties of tendons by breaking of peptide bonds in the
13 collagen molecules and rupture of the hydrogen bonds, although these changes
14 occur more often in the dry, rather than wet, state.

15
16 For the present FTIR results for unirradiated and 70 kGy irradiated bone
17 shown in Fig. 9, the infrared spectra in the region of 1585-1720 cm^{-1} are of
18 relevance as they show absorbance bands for the vibrations of protein amide I.
19 Among the underlying bands that make up the amide I spectral peak, two are of
20 particular interest, at $\sim 1660 \text{ cm}^{-1}$ and one at $\sim 1690 \text{ cm}^{-1}$, as it has been shown that
21 during collagen denaturing the relative intensity of the former decreases while
22 the latter increases [39, 66, 67]. Indeed, the ratio of these two bands corresponds
23 to the amount of enzymatic collagen cross-links present, specifically the non-
24 reducible mature Pyr cross-links (interfibrillar) and the reducible immature
25 DHNLN cross-links (intrafibrillar) found in bone [39]. In past studies, the
26 relative areas of 1660:1690 peaks were found to increase with aging in bovine
27 bone [39] and osteoporosis in human bone [66], while the ratio was found to
28 decrease with vitamin B₆-deficient chicken bone [39]. We similarly find here that
29 with 70 kGy of irradiation, the ratio of 1660:1690 peak areas decreases by almost
30 two-thirds, indicative of major changes in cross-linking and bonding in the
31 amide I region. With respect to the enzymatic cross-links in the collagen, the

1
2
3
4 decrease in this ratio with irradiation exposure suggests that there are changes in
5 the cross-link profile with a greater proportion of immature cross-links to the
6 mature cross-links following irradiation [65]; indeed, either an increase in
7 immature cross-links or a reduction in mature cross-links could disrupt the
8 integrity of the mature cross-links, such as covalent hydroxypyridinium, leading
9 to premature failure of the tissue.
10

11 Finally, we also find an increase in the concentration of the non-enzymatic
12 (AGE) cross-links (Fig. 10), which are known to suppress plasticity in older bone
13 [68, 69]. Indeed, we suspect that it is these cross-links that are primarily
14 responsible for the restriction in bone plasticity from fibrillar sliding in irradiated
15 bone. Although the increased accumulation of AGEs in aging bone can be
16 attributed to the longevity of the tissue and age-related changes in biological
17 bone metabolism (including incomplete tissue remodeling and altered glucose
18 metabolism), the mechanism of the apparent increased concentration of AGEs in
19 irradiated bone observed is not known. It may be possible that the non-
20 fluorescent intermediate cross-links that occur during the Amadori
21 rearrangement of sugars [40] is accelerated by irradiation, producing the
22 fluorescent AGEs observed here. It is also important to note that the quantitative
23 AGEs content is normalized with respect to collagen, and any loss of collagen
24 due to the damaging irradiation could also increase the AGEs per amount of
25 collagen. Regardless of the mechanism, however, the increase in AGEs content
26 is consistent with the inhibition of fibrillar sliding and loss of plastic toughening
27 observed in aging bone. These harmful effects of bone irradiation can be
28 observed at multiple length scales through the suppression of nano- and micro-
29 scale plasticity mechanisms, and may be the result of alterations in the profile
30 and distributions of the collagen cross-linking.
31
32
33
34
35
36
37
38
39
40
41
42
43
44
45
46
47
48
49
50
51
52
53
54
55
56
57
58
59
60
61
62
63
64
65

1
2
3
4
5
6
7
8
9
10
11
12
13
14
15
16
17
18
19
20
21
22
23
24
25
26
27
28
29
30
31
32
33
34
35
36
37
38
39
40
41
42
43
44
45
46
47
48
49
50
51
52
53
54
55
56
57
58
59
60
61
62
63
64
65

5. Conclusions

Based on an experimental study, spanning molecular to macroscopic length-scales, of the effects of synchrotron x-ray irradiation on the structure and mechanical properties of hydrated human cortical bone (in the transverse orientation), the following conclusions can be made:

1. Compared to healthy (unirradiated) bone, exposure to irradiation doses between 0.05 and 630 kGy progressively led to a severe degradation in strength, ductility and toughness.
2. After 630 kGy of radiation, the ultimate strength and ductility were decreased by ~80%, the work-of-fracture by ~100%, and the fracture toughness (fracture resistance) by a factor of five. No major changes in the mechanical integrity of the bone could be discerned for irradiation exposures of 35 kGy or less.
3. The irradiation-induced loss in fracture resistance is attributed to both intrinsic (plasticity) and extrinsic (shielding) contributions to the bone toughness. Compared to unirradiated bone, fracture in irradiation-damaged bone was characterized by far smaller crack-path deflections, smoother fracture surfaces, and hence much lower extrinsic toughening.
4. At irradiation doses of 70 kGy and above, stress-strain curves displayed a complete absence of post-yield plastic deformation and, with increasing irradiation, a major reduction in fracture load and toughness. The irradiation-induced suppression of bone plasticity acts to severely limit the intrinsic toughness by macroscopically embrittling the bone tissue.
5. Such irradiation-induced suppression of bone plasticity is consistent with SAXS/WAXD studies of the partitioning of strain in the bone under load, which indicated that for an applied tissue strain of ~1%, the individual strain carried by the collagen fibrils was some 40% smaller in 70 kGy irradiated

1
2
3
4 bone, as compared to unirradiated bone, indicative of a lack of plasticity in
5 the collagen.
6

- 7
8
9
10
11
12
13
14
15
16
17
18
19
20
21
22
23
24
25
26
27
28
29
30
31
32
33
34
35
36
37
38
39
40
41
42
43
6. The loss in intrinsic toughness through the suppression of plasticity via the mechanism of fibrillar sliding is attributed to an increased incidence of specific cross-linking of the collagen with irradiation. Measurements for unirradiated and 70 kGy irradiated bone revealed that there was a ~21% increase in the concentration of non-enzymatic cross-links, in the form of advanced glycation end-products (AGEs), in the irradiated bone, which acts to restrict fibrillar sliding of the collagen fibrils.
 7. With respect to the enzymatic cross-links, we find a decreasing ratio of non-reducible (mature) to reducible (immature) cross-links in the collagen in irradiation-damaged bone. The departure from the healthy distribution of these cross-links appears to progressively disrupt the integrity of the mature cross-links, leading to lower fracture loads.
 8. At very large exposure of 630 kGy, the distortion of the UV Raman spectra further suggests complete fracture of peptide bonds in the collagen backbone, which is consistent with the progressively degraded bone strength at high irradiation exposures.

44 **Acknowledgements**

45
46
47 This work was supported by the National Institute of Health (NIH/NIDCR)
48 under grant no. 5R01 DE015633 to the Lawrence Berkeley National Laboratory
49 (LBNL); support for S.Y.T. and T.A. was additionally provided by NIH grants
50 no. R01DE019284 and F32AR059497. We acknowledge the use of the two x-ray
51 synchrotron beam lines 7.3.3 (SAXS/WAXD) and 8.3.2 (micro-tomography) at the
52 Advanced Light Source at the Lawrence Berkeley National Laboratory (LBNL),
53 which is supported by the Office of Science of the U.S. Department of Energy
54
55
56
57
58
59
60
61
62
63
64
65

1
2
3
4
5
6
7
8
9
10
11
12
13
14
15
16
17
18
19
20
21
22
23
24
25
26
27
28
29
30
31
32
33
34
35
36
37
38
39
40
41
42
43
44
45
46
47
48
49
50
51
52
53
54
55
56
57
58
59
60
61
62
63
64
65

under contract no. DE-AC02-05CH11231. The authors wish to thank Drs. Tony Tomsia, Maximilien Launey, Joel Ager, Hans Bechtel, Alex Hexemer, Andrew Tauschera, and Alastair MacDowell at LBNL for their considerable help, and Professor Tony Keaveny and Mike Jekir, of the Mechanical Engineering Department at the University of California, Berkeley, for graciously allowing us to use their facilities to machine samples for this project.

References

- [1] Fratzl P, Weinkamer R. Nature's hierarchical materials. *Prog Mater Sci* 2007;52:1263-1334.
- [2] Meyers MA, Chen PY, Lin AYM, Seki Y. Biological materials: structure and mechanical properties. *Prog Mater Sci* 2008;53:1-206.
- [3] Rho JY, Kuhn-Spearing L, Zioupos P. Mechanical properties and the hierarchical structure of bone. *Med Engin Phys* 1998;20:92-102.
- [4] Weiner S, Wagner HD. The material bone: Structure mechanical function relations. *Annu Rev Mater Sci* 1998;28:271-298.
- [5] Ritchie RO, Buehler MJ, Hansma PK. Plasticity and toughness in bone. *Phys Today* 2009;62:41-47.
- [6] Launey ME, Buehler MJ, Ritchie RO. On the mechanistic origins of toughness in bone. *Annu Rev Mater Res* 2010;40:25-53.
- [7] Ritchie RO. Mechanisms of fatigue crack propagation in metals, ceramics and composites: role of crack tip shielding. *Mater Sci Eng A* 1988;103:15-83.
- [8] Ritchie RO. Mechanisms of fatigue-crack propagation in ductile and brittle solids. *Int J Fract* 1999;100:55-83.
- [9] Ji B, Gao H. Mechanical properties of nanostructure of biological materials. *J Mech Phys Solids* 2004;52:1963-1990.
- [10] Gupta HS, Seto J, Wagermaier W, Zaslansky P, Boesecke P, Fratzl P. Cooperative deformation of mineral and collagen in bone at the nanoscale. *Proc Natl Acad Sci* 2006;103:17741-17746.
- [11] Koester KJ, Ager JW, Ritchie RO. The true toughness of human cortical bone measured with realistically short cracks *Nat Mater*. 2008;7:672-677.
- [12] Koester KJ, Barth HD, Ritchie RO. Effect of aging on the transverse toughness of human cortical bone: evaluation by R-curves. *J Mech Behav Biomed Mater* 2011;4:1504-1513.

- 1
2
3
4
5
6 [13] Weiner S, Traub W, Wagner HD. Lamellar bone: structure-function relations. *J*
7 *Struct Biol* 1999;126:241-255.
8
9
10 [14] Wagner HD, Weiner S. On the relationship between the microstructure of bone
11 and its mechanical stiffness. *J Biomech* 1992;25:1311-1320.
12
13
14 [15] Wagermaier W, Gupta HS, Gourrier A, Paris O, Roschger P, Burghammer M, et
15 al. Scanning texture analysis of lamellar bone using microbeam synchrotron X-
16 ray radiation. *J Appl Crystallogr* 2007;40:115-120.
17
18
19 [16] Wasserman N, Brydges B, Searles S, Akkus O. In vivo linear microcracks of
20 human femoral cortical bone remain parallel to osteons during aging. *Bone*
21 2008;43:856-861.
22
23
24 [17] Peterlik H, Roschger P, Klaushofer K, Fratzl P. From brittle to ductile fracture of
25 bone. *Nat Mater* 2006;5:52-55.
26
27
28
29 [18] Vangsness CT, Garcia IA, Mills CR, Kainer MA, Roberts MR, Moore TM.
30 Allograft transplantation in the knee: tissue regulation, procurement, processing,
31 and sterilization. *Am J Sports Med* 2003;31:474-481.
32
33
34 [19] Cheung DT, Perelman N, Tong D, Nimni ME. The effect of gamma-irradiation on
35 collagen molecules, isolated alpha-chains, and crosslinked native fibers. *J Biomed*
36 *Mater Res* 1990;24:581-589.
37
38
39 [20] Grieb TA, Forng R-Y, Bogdansky S, Ronholdt C, Parks B, Drohan WN, Burgess
40 WH, Lin J. High-dose gamma irradiation for soft tissue allografts: high margin of
41 safety with biomechanical integrity. *J Orthop Res* 2006;24:1011-1018.
42
43
44 [21] Nguyen H, Morgan D, Forwood M. Sterilization of allograft bone: effects of
45 gamma irradiation on allograft biology and biomechanics. *Cell Tissue Banking*
46 2007;8:93-105.
47
48
49 [22] Salehpour A, Butler DL, Proch FS, Schwartz HE, Feder SM, Doxey CM, et al.
50 Dose-dependent response of gamma irradiation on mechanical properties and
51 related biochemical composition of goat bone-patellar tendon-bone allografts. *J*
52 *Orthop Res* 1995;13:898-906.
53
54
55
56
57
58
59
60
61
62
63
64
65

- 1
2
3
4 [23] Barth HD, Launey ME, MacDowell AA, Ager III JW, Ritchie RO. On the effect of
5 X-ray irradiation on the deformation and fracture behavior of human cortical
6 bone. *Bone* 2010;46:1475-1485.
7
8
9
10 [24] Akhtar R, Daymond MR, Almer JD, Mummery PM. Elastic strains in antler
11 trabecular bone determined by synchrotron x-ray diffraction. *Acta Biomater*
12 2008;4:1677-1687.
13
14
15 [25] Deymier-Black AC, Almer JD, Stock SR, Haeffner DR, Dunand DC. Synchrotron
16 x-ray diffraction study of load partitioning during elastic deformation of bovine
17 dentin. *Acta Biomater* 2010;6:2172-2180.
18
19
20
21 [26] Almer JD, Stock SR. Internal strains and stresses measured in cortical bone via
22 high-energy x-ray diffraction. *J Struct Biol* 2005;152:14-27.
23
24
25
26 [27] Thurner PJ, Wyss P, Voide R, Stauber M, Stampanoni M, Sennhauser U, et al.
27 Time-lapsed investigation of three-dimensional failure and damage
28 accumulation in trabecular bone using synchrotron light. *Bone* 2006;39:289-299.
29
30
31
32 [28] Voide R, Schneider P, Stauber M, Wyss R, Stampanoni M, Sennhauser U, et al.
33 Time-lapsed assessment of microcrack initiation and propagation in murine
34 cortical bone at submicrometer resolution. *Bone* 2009;45:164-173.
35
36
37 [29] Ager III JW, Nalla RK, Breeden KL, Ritchie RO. Deep-ultraviolet Raman
38 spectroscopy study of the effect of aging on human cortical bone. *J Biomed Opt*
39 2005;10:034012.
40
41
42
43 [30] ASTM standard E1820-09. Standard test method for measurement of fracture
44 toughness. West Conshohocken, PA, USA: American Society for Testing and
45 Materials. 2009.
46
47
48
49 [31] Yan JH, Mecholsky JJ, Clifton KB. How tough is bone? application of elastic-
50 plastic fracture mechanics to bone. *Bone* 2007;40:479-484.
51
52
53 [32] Launey ME, Chen PY, McKittrick J, Ritchie RO. Mechanistic aspects of the
54 fracture toughness of elk antler bone. *Acta Biomater* 2010;6:1505-1514.
55
56
57 [33] Kinney JH, Nichols MC. X-ray tomographic microscopy using synchrotron
58 radiation. *Annu Rev Mater Sci* 1992;22:121-152.
59
60
61
62
63
64
65

- 1
2
3
4
5 [34] Vlassenbroeck J, Dierick M, Masschaele B, Cnudde V, Van Hoorebeke L, Jacobs
6 P. Software tools for quantification of x-ray microtomography at the 'Center for
7 X-ray Tomography' at Ghent University. Nucl Instru Meth Physics Res A
8 2007;580:442-445.
9
- 10
11 [35] Mercury CS. Avizo™ 3D visualization framework: Chelmsford, MA. 2008.
12
13
- 14 [36] van de Weert M, van 't Hof R, van der Weerd J, Heeren RMA, Posthuma G,
15 Hennink WE, et al. Lysozyme distribution and conformation in a biodegradable
16 polymer matrix as determined by FTIR techniques. J Controlled Release
17 2000;68:31-40.
18
19
- 20
21 [37] George A, Veis A. FTIRS in water demonstrates that collagen monomers undergo
22 a conformational transition prior to thermal self-assembly in vitro. Biochem
23 1991;30:2372-2377.
24
25
- 26
27 [38] Paschalis E, Mendelsohn R, Boskey A. Infrared assessment of bone quality: a
28 review. Clin Orthop Relat Res 2011;469:2170-2178.
29
30
- 31 [39] Paschalis EP, Verdellis K, Doty SB, Boskey AL, Mendelsohn R, Yamauchi M.
32 Spectroscopic characterization of collagen cross-links in bone. J Bone Miner Res
33 2001;16:1821-1828.
34
35
- 36
37 [40] Bailey AJ. Molecular mechanisms of ageing in connective tissues. Mech Ageing
38 Dev 2001;122:735-755.
39
40
- 41 [41] Woessner JF. The determination of hydroxyproline in tissue and protein samples
42 containing small proportions of this imino acid. Arch Biochem Biophys
43 1961;93:440-447.
44
45
- 46
47 [42] Anderson MJ, Keyak JH, Skinner HB. Compressive mechanical-properties of
48 human cancellous bone after gamma irradiation. J Bone Jt Surg Am Vol 1992;
49 4A:747-752.
50
51
- 52
53 [43] Currey JD, Foreman J, Laketic I, Mitchell J, Pegg DE, Reilly GC. Effects of
54 ionizing radiation on the mechanical properties of human bone. J Orthop Res
55 1997;15:111-117.
56
57
58
59
60
61
62
63
64
65

- 1
2
3
4
5 [44] Fideler BM, Vangsness T, Lu B, Orlando C, Moore T. Gamma irradiation effects
6 on biomechanical properties of human bone - patellar tendon - bone allografts.
7 Am J Sports Med 1995;23:643-646.
8
9
10 [45] Gibbons MJ, Butler DL, Grood ES, Bylskiaustrow DI, Levy MS, Noyes FR. Effects
11 of gamma irradiation on the initial mechanical and material properties of goat
12 bone - patellar tendon - bone allografts. J Orthop Res 1991;9:209-218.
13
14
15 [46] Hamer AJ, Strachan JR, Black MM, Ibbotson CJ, Stockley I, Elson RA.
16 Biomechanical properties of cortical allograft bone using a new method of bone
17 strength measurement - a comparison of fresh, fresh-frozen and irradiated bone.
18 J Bone Jt Surg Br Vol 1996;78B:363-368.
19
20
21 [47] Hamer AJ, Stockley I, Elson RA. Changes in allograft bone irradiated at different
22 temperatures. J Bone Jt Surg 1999;81:342-345.
23
24
25 [48] Nalla RK, Kinney JH, Ritchie RO. Mechanistic fracture criteria for the failure of
26 human cortical bone. Nat Mater 2003;2:164-168.
27
28
29
30 [49] Akkus O, Belaney RM, Das P. Free radical scavenging alleviates the
31 biomechanical impairment of gamma radiation sterilized bone tissue. J Orthop
32 Res 2005;23:838-845.
33
34
35 [50] Thompson JB, Kindt JH, Drake B, Hansma HG, Morse DE, Hansma PK. Bone
36 indentation recovery time correlates with bond reforming time. Nature
37 2001;414:773-776.
38
39
40 [51] Fantner GE, Hassenkam T, Kindt JH, Weaver JC, Birkedal H, Pechenik L, et al.
41 Sacrificial bonds and hidden length dissipate energy as mineralized fibrils
42 separate during bone fracture. Nat Mater 2005;4:612-616.
43
44
45 [52] Krauss S, Fratzl P, Seto J, Currey JD, Estevez JA, Funari SS, et al. Inhomogeneous
46 fibril stretching in antler starts after macroscopic yielding: Indication for a
47 nanoscale toughening mechanism. Bone 2009;44:1105-1110.
48
49
50 [53] Gupta H, Wagermaier W, Zickler G, Hartmann J, Funari S, Roschger P, et al.
51 Fibrillar level fracture in bone beyond the yield point. Int J Fract 2006;139:425-
52 436.
53
54
55
56
57
58
59
60
61
62
63
64
65

- 1
2
3
4 [54] Harrington MJ, Gupta HS, Fratzl P, Waite JH. Collagen insulated from tensile
5 damage by domains that unfold reversibly: in situ X-ray investigation of
6 mechanical yield and damage repair in the mussel byssus. *J Struct Biol* 2009;
7 67:47-54.
8
9
10
11 [55] Bailey AJ, Sims TJ, Ebbesen EN, Mansell JP, Thomsen JS, Mosekilde L. Age-
12 related changes in the biochemical properties of human cancellous bone collagen:
13 relationship to bone strength. *Calcif Tissue Int* 1999;65:203-210.
14
15
16 [56] Banse X, Sims TJ, Bailey AJ. Mechanical properties of adult vertebral cancellous
17 bone: correlation with collagen intermolecular cross-links. *J Bone Miner Res*
18 2002;17:1621-1628.
19
20
21 [57] Viguet-Carrin S, Garnero P, Delmas P. The role of collagen in bone strength.
22 *Osteoporosis Int* 2006;17:319-336.
23
24
25 [58] Wang X, Shen X, Li X, Mauli Agrawal C. Age-related changes in the collagen
26 network and toughness of bone. *Bone* 2002;31:1-7.
27
28
29 [59] Knott L, Bailey AJ. Collagen cross-links in mineralizing tissues: a review of their
30 chemistry, function, and clinical relevance. *Bone* 1998;22:181-187.
31
32
33 [60] Buehler MJ. Nanomechanics of collagen fibrils under varying cross-link
34 densities: Atomistic and continuum studies. *J Mech Behav Biomed Mater*
35 2008;1:59-67.
36
37
38 [61] Buehler MJ. Multiscale aspects of mechanical properties of biological materials. *J*
39 *Mech Behav Biomed Mater* 2011;4:125-127.
40
41
42 [62] Jäger I, Fratzl P. Mineralized collagen fibrils: A mechanical model with a
43 staggered arrangement of mineral particles. *Biophys J* 2000; 79: 1737-1746.
44
45
46 [63] Gupta HS, Wagermaier W, Zickler GA, Raz-Ben Aroush D, Funari SS, Roschger
47 P, et al. Nanoscale deformation mechanisms in bone. *Nano Lett* 2005; 5: 2108-
48 2111.
49
50
51 [64] Colwell A, Hamer A, Blumsohn A, Eastell R. To determine the effects of
52 ultraviolet light, natural light and ionizing radiation on pyridinium cross-links in
53 bone and urine using high-performance liquid chromatography. *Eur J Clin Invest*
54 1996;26:1107-1114.
55
56
57
58
59
60
61
62
63
64
65

- 1
2
3
4
5
6 [65] Bailey AJ, Rhodes DN, Cater CW. Irradiation-induced crosslinking of collagen.
7 Radiat Res 1964;22:606-621.
8
9
10 [66] Paschalis EP, Shane E, Lyritis G, Skarantavos G, Mendelsohn R, Boskey AL. Bone
11 fragility and collagen cross-links. J Bone Miner Res 2004;19:2000-2004.
12
13
14 [67] Saito M, Marumo K. Collagen cross-links as a determinant of bone quality: a
15 possible explanation for bone fragility in aging, osteoporosis, and diabetes
16 mellitus. Osteoporosis Int 2010;21:195-214.
17
18
19
20 [68] Vashishth D, Gibson GJ, Khoury JI, Schaffler MB, Kimura J, Fyhrie DP. Influence
21 of nonenzymatic glycation on biomechanical properties of cortical bone. Bone
22 2001;28:195-201.
23
24
25
26 [69] E A Zimmermann ES, H Bale, HD Barth, S Tang, P Reichert, B Busse, et al. Age-
27 related changes in the plasticity and toughness of human cortical bone at
28 multiple length-scales. Proc Natl Acad Sci 2011; in press.
29
30
31
32
33
34
35
36
37
38
39
40
41
42
43
44
45
46
47
48
49
50
51
52
53
54
55
56
57
58
59
60
61
62
63
64
65

List of Figure Captions

Figure 1: The structural hierarchy of bone. At the smallest level, at the scale of the tropocollagen molecules and mineralized collagen fibrils, (intrinsic) toughening is achieved through plasticity, principally via mechanisms of molecular uncoiling and intermolecular sliding of molecules and mineralized collagen fibrils. Cross-links form at these length-scales between the collagen molecules and between the fibrils [40]. At micrometer dimensions, the breaking of sacrificial bonds at the interfaces of fibril arrays contributes to increased energy dissipation, together with crack bridging of microcracks by collagen fibrils. At the largest length-scales in the range of 10s to 100s μm , the primary sources of toughening are extrinsic and result from extensive crack deflection and crack bridging/twisting by uncracked ligaments, both mechanisms that are motivated by the occurrence of microcracking [5, 6].

Figure 2: Schematic showing the beamline setup for *in situ* tensile testing of bone with real time small-angle x-ray scattering and wide-angle x-ray diffraction (SAXS/WAXD) imaging. The 10 keV x-ray beam penetrates the longitudinally oriented human cortical bone sample perpendicular to the tensile set up. The SAXS detector is positioned to record the meridional D -spacing in the staggered array of mineralized collagen fibrils. The WAXD detector is positioned to record patterns from the crystallites with c -axis along the tensile direction. Tissue strain is determined by the marker lines on the sample (camera not shown in schematic). Images (a) and (b) show WAXD pattern and the SAXS pattern of bone respectively, with the region for azimuthal integration shown in the pie-shaped sector outlined in both. Figures (c) and (d) show the integrated intensity variation over this region. Graph (c) shows a pronounced (0002) diffraction peak for the hydroxyapatite, and graph (d) shows a pronounced first order diffraction peak due to the fibrillar D -spacing (67 nm).

Figure 3: Mechanical properties of hydrated human cortical bone (transverse orientation) subjected to varying degrees of x-ray irradiation. (a) Stress-strain curves from three-point bending tests (offset for clarity) and (b) fracture toughness R-curves showing resistance to fracture in terms of the stress intensity, K_I , as a function of crack extension, Δa , both as a function of prior x-irradiation dosage. K_I fracture toughness values were back-calculated from J measurements using the J - K equivalence for mode I fracture. The end of the curves indicates the critical toughness values, K_{Ic} , at which complete failure occurred.

Figure 4: X-ray computed micro tomography of crack paths in hydrated human cortical bone in the transverse orientation following (a-c) low dose (50 Gy), and (e-g) high dose (~MGy) x-irradiation. Images show crack paths: (a) & (d) x-ray tomographs from side-view perpendicular to the crack plane, (b) & (e) 3-D x-ray tomography images of these paths (3-D crack surface is in purple; Haversian canals are yellow), and (c) & (f) 2-D tomographs of the paths from the back face of the sample. The crack deflects on encountering the osteons; such crack deflection and crack twisting is the prime extrinsic toughening mechanism in bone in the transverse orientation. Note, however, that the frequency of such deflections increases with irradiation while their severity decreases, resulting in less meandering crack paths in the irradiated bone.

Figure 5: Partitioning of strain between the collagen and mineral as a function of the global tissue strain in 70 kGy irradiated vs. unirradiated hydrated human cortical bone. Variation of the strain from SAXS/WAXD measurements in the (a) collagen and (b) mineral as a function of the global applied strain in the bone tissue for unirradiated and 70 kGy irradiated bone. The collagen and mineral strain are binned in regular intervals of tissue strain ($N=20$ for each group). Error bars in the graphs are standard deviation of the binned value. Note that for a given strain in the bone tissue the strain in the collagen fibrils is diminished in irradiated vs. unirradiated bone, consistent with the progressive loss in macroscopic plasticity in bone with increasing irradiation.

Figure 6: Strain in collagen fibril, and mineral in bone as a function of applied strain in the tissue for human cortical bone in the (a) unirradiated and (b) 70 kGy irradiated condition. The upper graphs show the ratios of fibril to tissue strain, ϵ_F/ϵ_T , and mineral to tissue strain, ϵ_M/ϵ_T , for the (a) unirradiated and (b) 70 kGy irradiated bone, averaged from $N=20$ samples for each group. In (a) and (b), the solid lines represent the constant strain ratio expected before yield. In (a), the dotted line represents where the ratio would vary if the fibril and mineral strain remained constant beyond the yield strain. The lower graphs show the corresponding stress-strain curves for the (a) unirradiated and (b) 70 kGy irradiated human cortical bone.

Figure 7: (a) Schematic illustration of the sample orientation in relation to the bone-matrix microstructure in human cortical bone (top) and schematic model for bone deformation for the various hierarchical length-scales in response to external tensile load. Strain is simultaneously measured at all three levels of the structural hierarchy (tissue, fibril, and mineral nanoparticles). The mineralized fibrils, which are stiffened with collagen cross-links, deform in tension and transfer the stress between neighboring fibrils by shearing in the thin layer of the matrix. Within each mineralized fibril, the stiff mineral platelets deform in tension and transfer stresses between adjacent platelets by shearing in the interparticle collagen matrix. (Red lines demonstrate shearing

qualitatively). (Adapted from ref. [10]) (b) At a fixed tissue strain of 0.85%, the individual strain in the fibrils is 42% less in the 70 kGy irradiated bone than in the healthy unirradiated bone.

Figure 8: UV-Raman spectroscopy of (hydrated) unirradiated and x-irradiated human cortical bone. (a) UV-Raman spectra for five different irradiation groups after doses of 0, 0.05, 70, 210 and 650 kGy, showing specifically the large changes in the relative height of the amide I feature compared to the CH₂ wag peak. The amide I (primarily from C=O stretch) peak has previously been a good indicator for observing changes in the protein arrangement as the amide is known to play a role in cross-linking and bonding. The amide I peak height of the peak monotonically increases with irradiation, consistent with an increase in cross-linking in the collagen. Some of the other noticeable organic features for the bone matrix are the CH₂ wag peak (1454-1461 cm⁻¹), amide III (primarily from in-phase combination of NH in-plane bend and CN stretch, 1245-1260 cm⁻¹), and amide II (primarily from out of phase combination of NH in-plane bend and CN stretch). (Additional data from ref. [23]).

Figure 9: Fourier transform infrared spectroscopy of human cortical bone in the unirradiated and 70 kGy irradiated condition. (a) Shows a comparison of the calculated spectroscopic ratio of the 1660:1690 cm⁻¹ peaks in unirradiated and 70 kGy irradiated samples. The 1660:1690 ratios are calculated through a combination of second derivative spectroscopy to locate the position of the underlying bands within the amide I region and then peak fitting of these subbands to determine the relative percent area of each underlying component. The area 1660:1690 ratio appears to correspond to the ratio of nonreducible/reducible collagen cross-links in bone [39]. Following irradiation of 70 kGy, the 1660:1690 ratio decreases by almost a third. (b) Shows FTIR spectra and the amide I underlying bands for both groups.

Figure 10: The accumulation of advanced glycation end-products (AGEs) was fluorimetrically quantified in the cortex of the femora in unirradiated and 70 kGy irradiated human cortical bone samples. AGEs increase slightly when bone is irradiated with a dose of 70 kGy which increased the concentration of fluorescent (non-enzymatic) cross-links to ~21% more than in the unirradiated bone.

Figure 1
[Click here to download high resolution image](#)

Structure of Cortical Bone

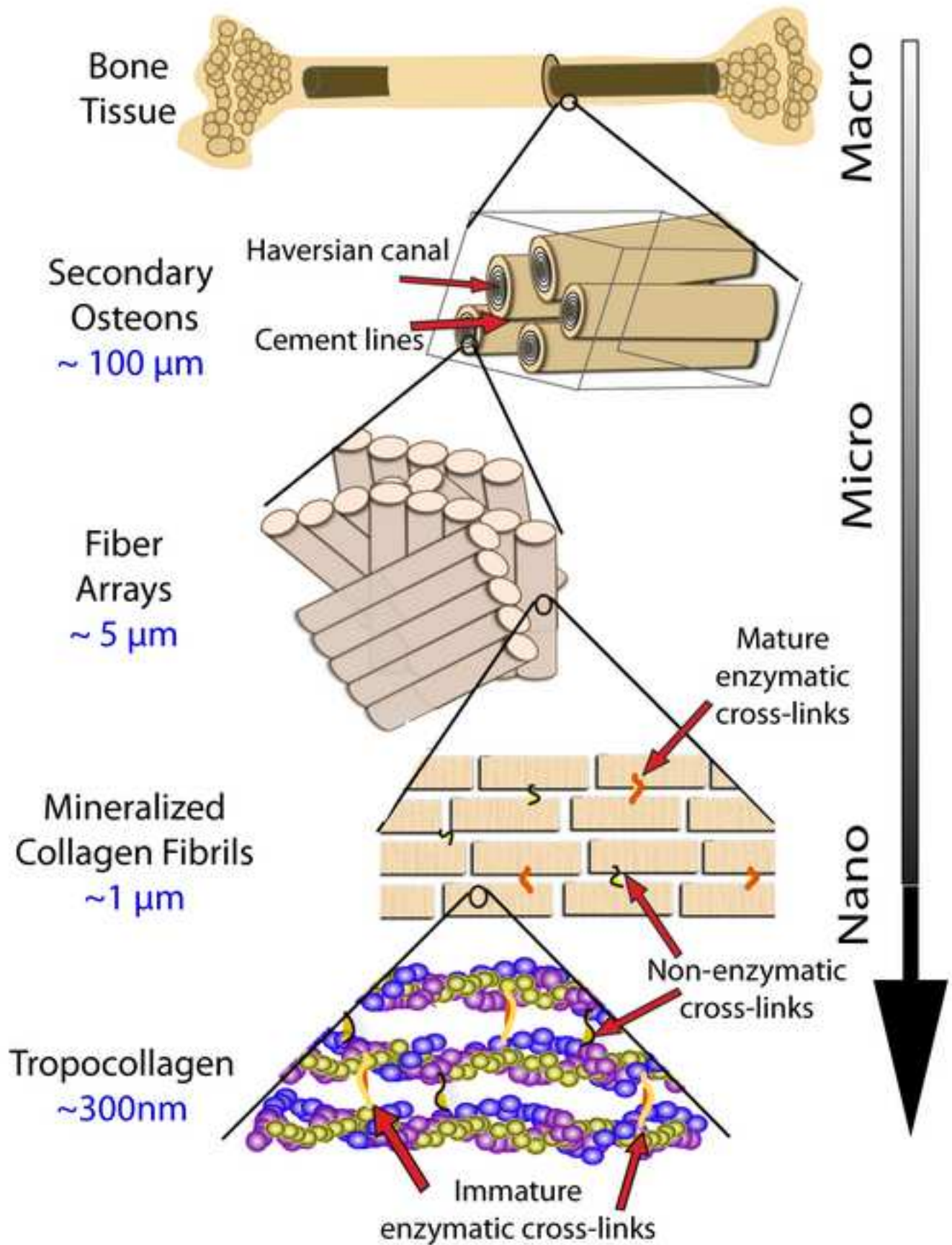


Figure 2
[Click here to download high resolution image](#)

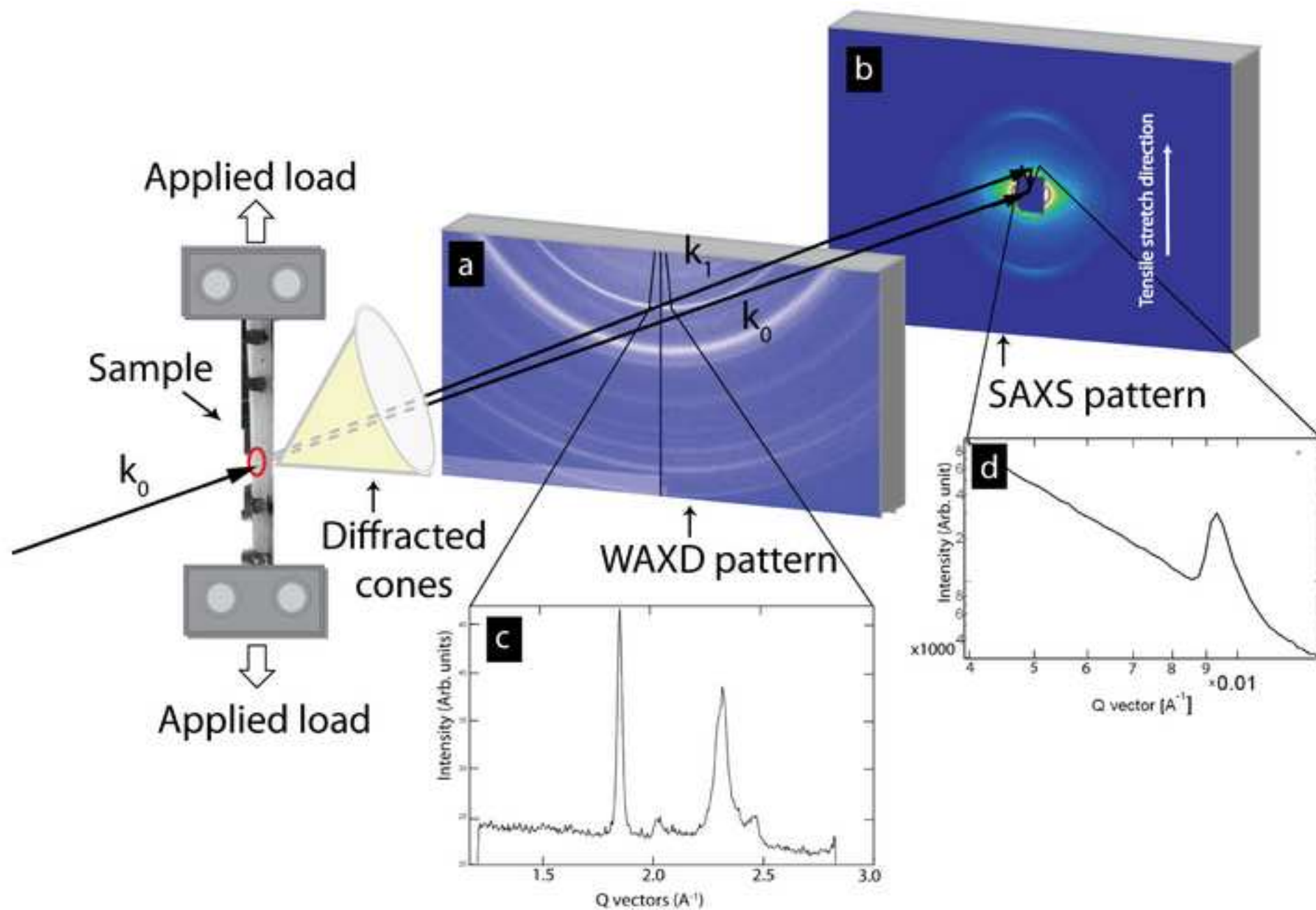


Figure 3
[Click here to download high resolution image](#)

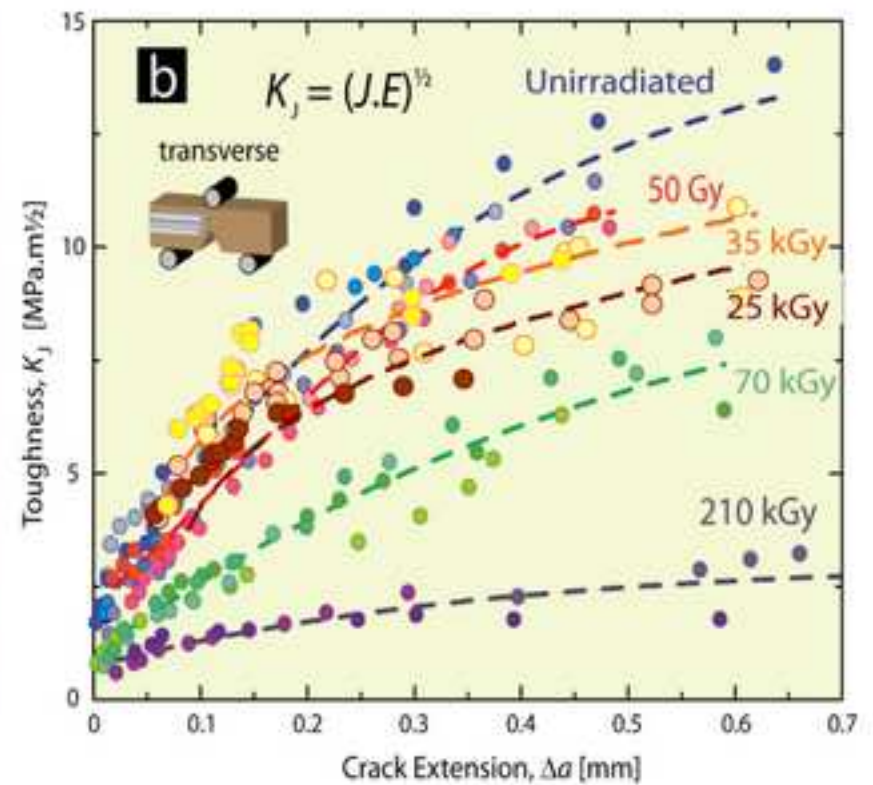
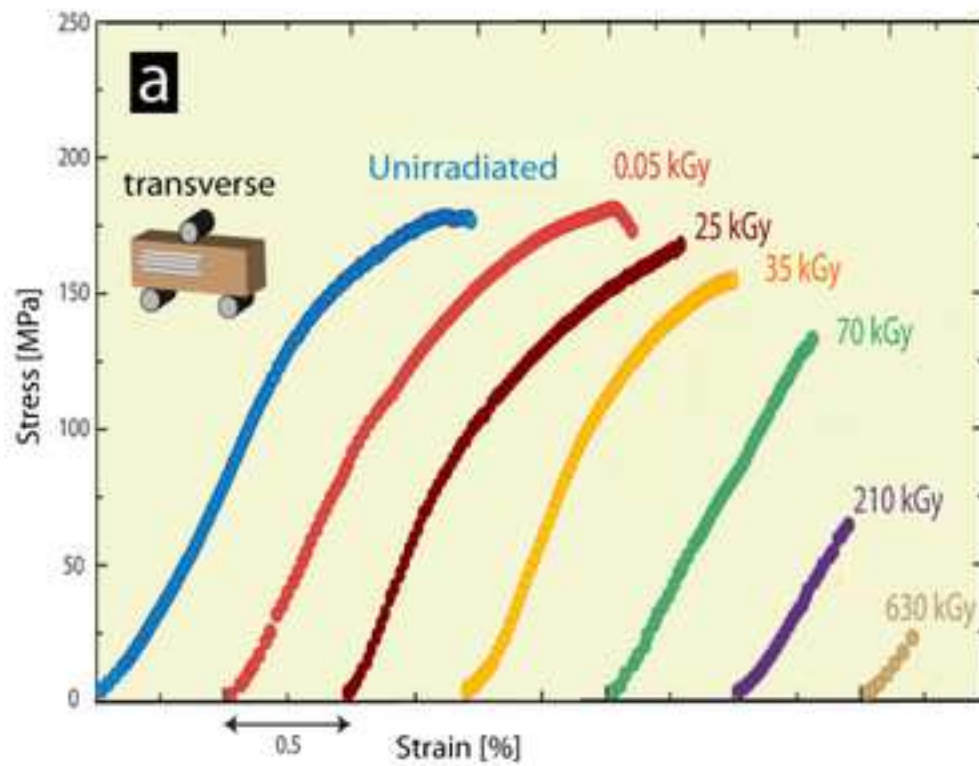
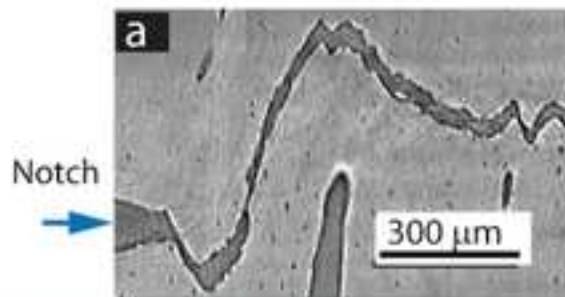


Figure 4
[Click here to download high resolution image](#)

Low Dose (50 Gy) Irradiated Bone



High Dose (~MGy) Irradiated Bone

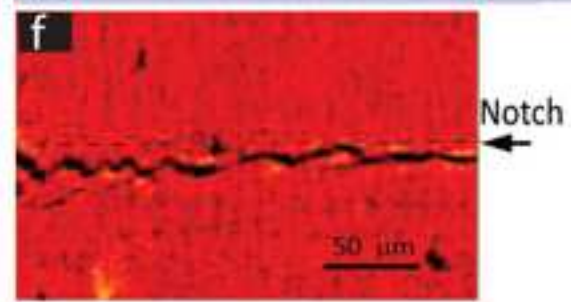
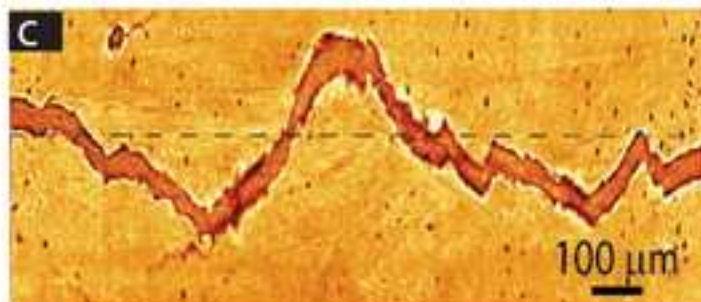
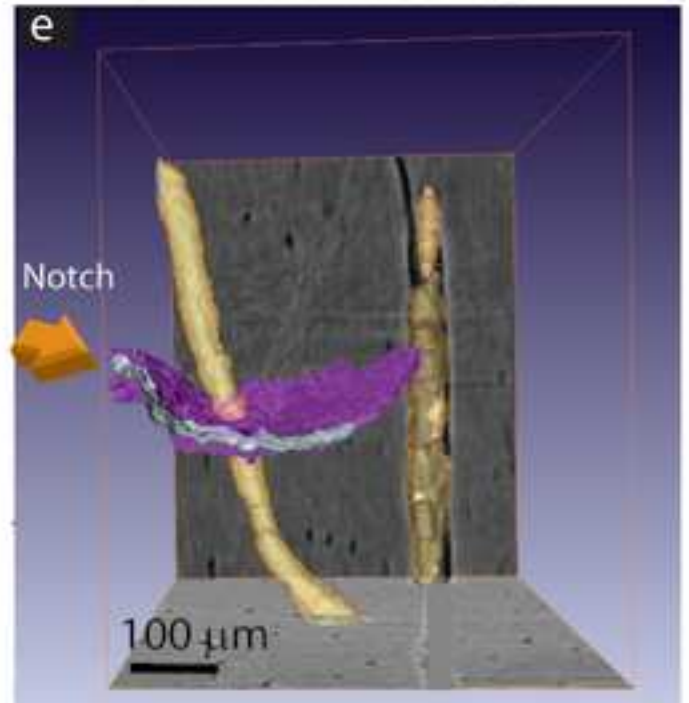
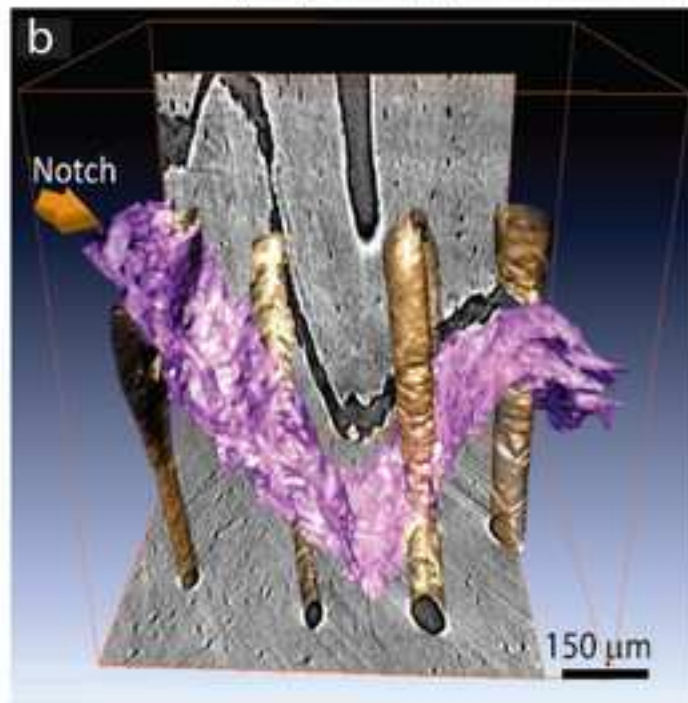
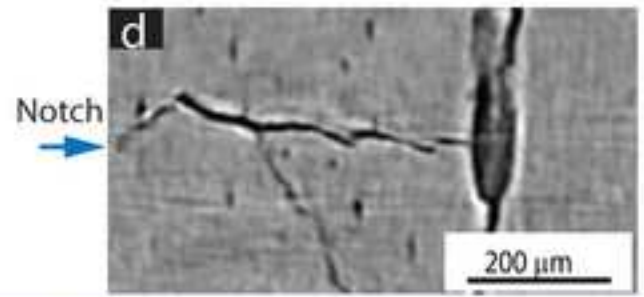


Figure 5
[Click here to download high resolution image](#)

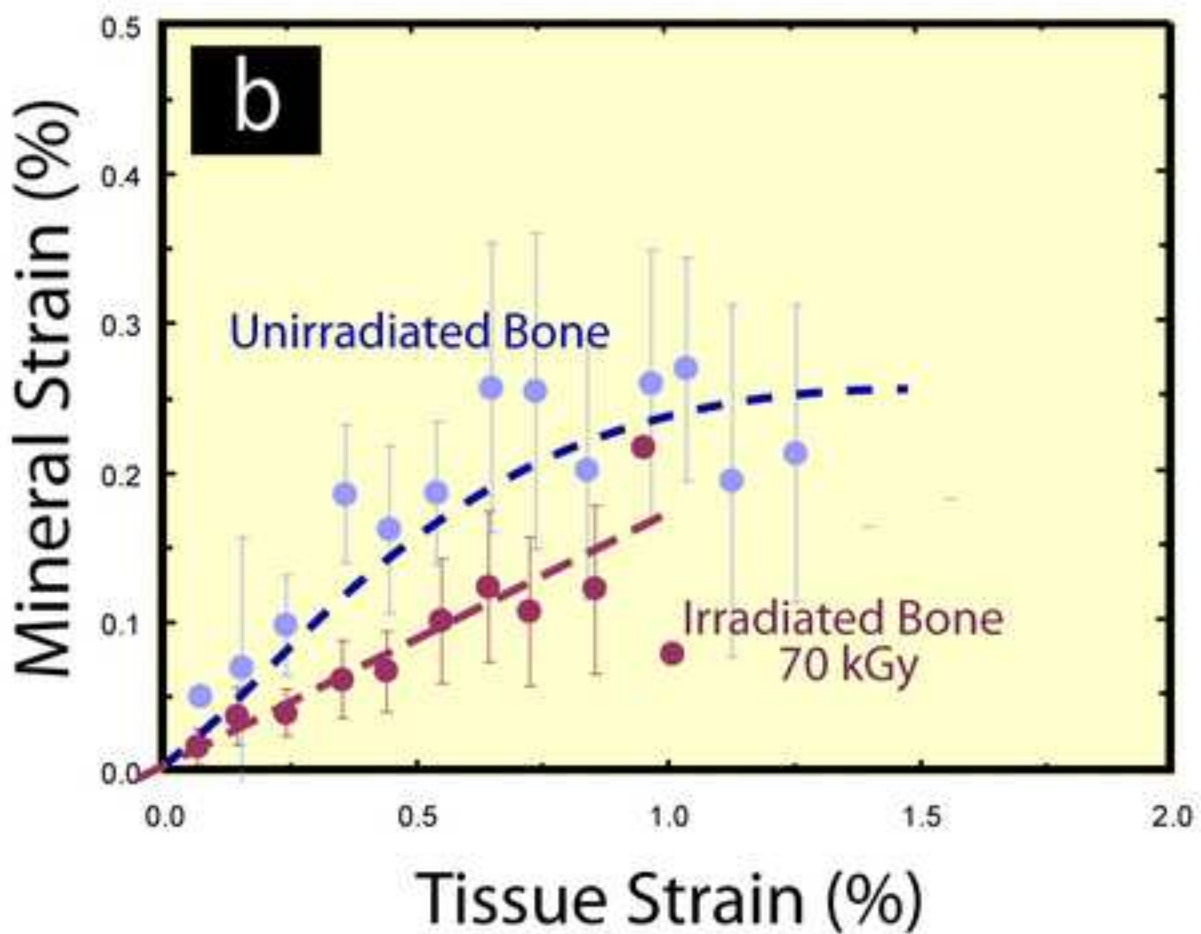
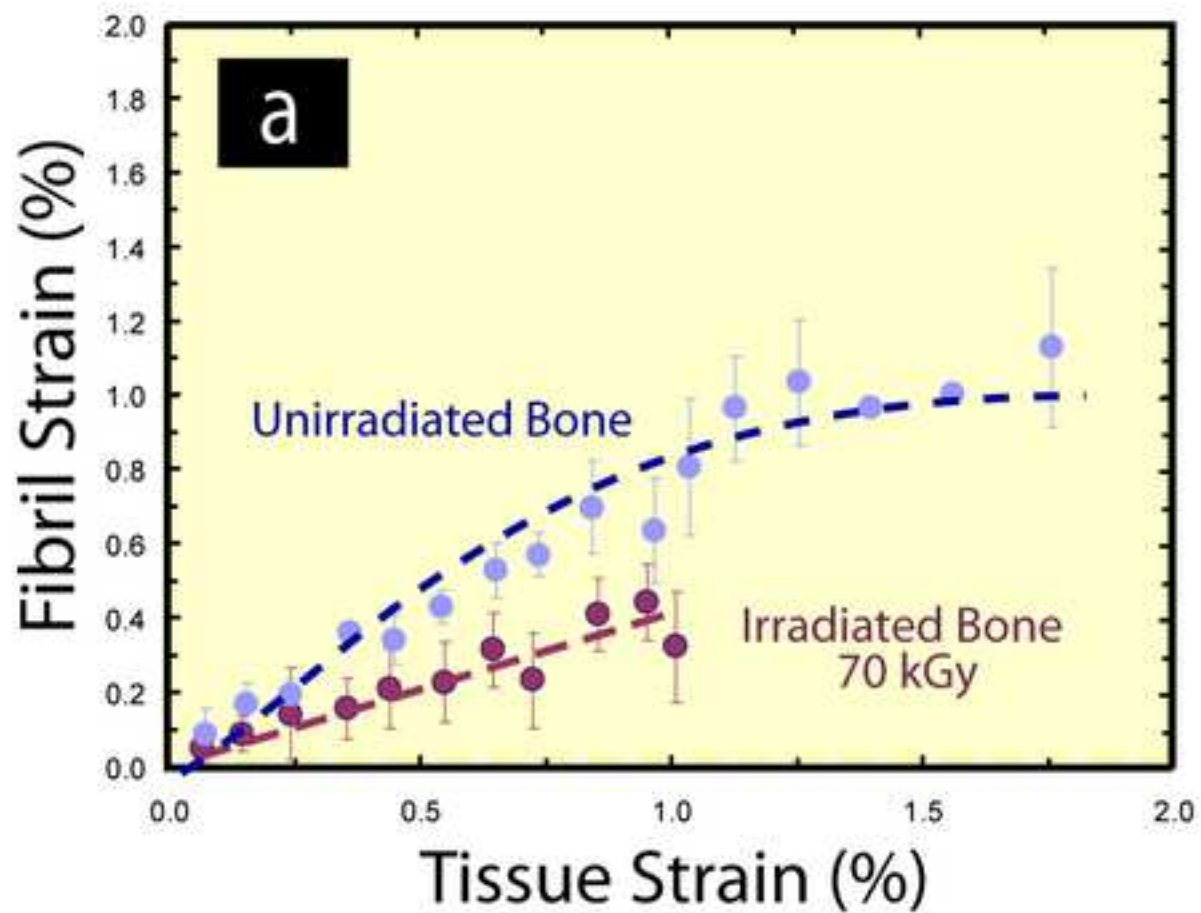


Figure 6
[Click here to download high resolution image](#)

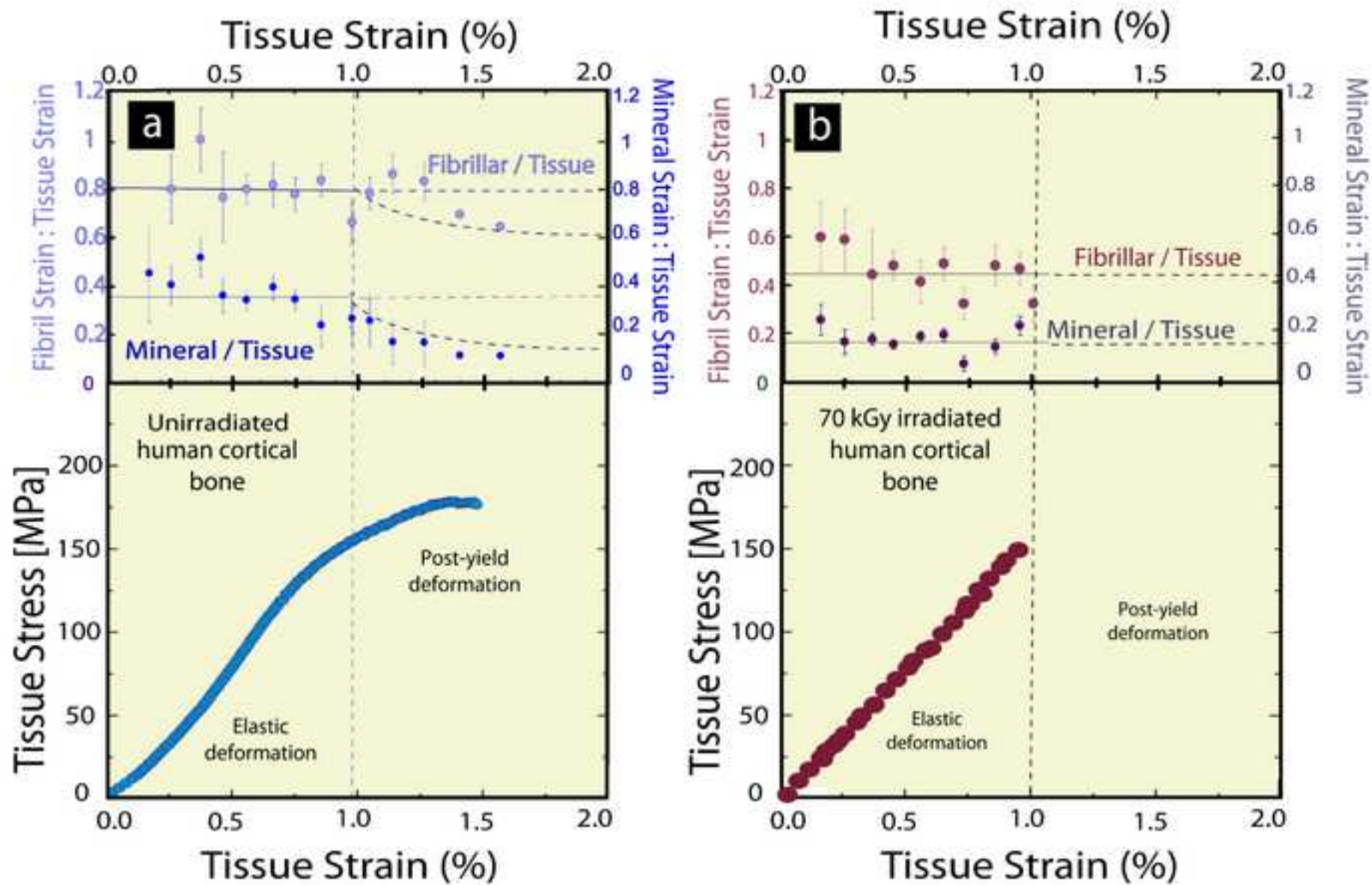


Figure 7
[Click here to download high resolution image](#)

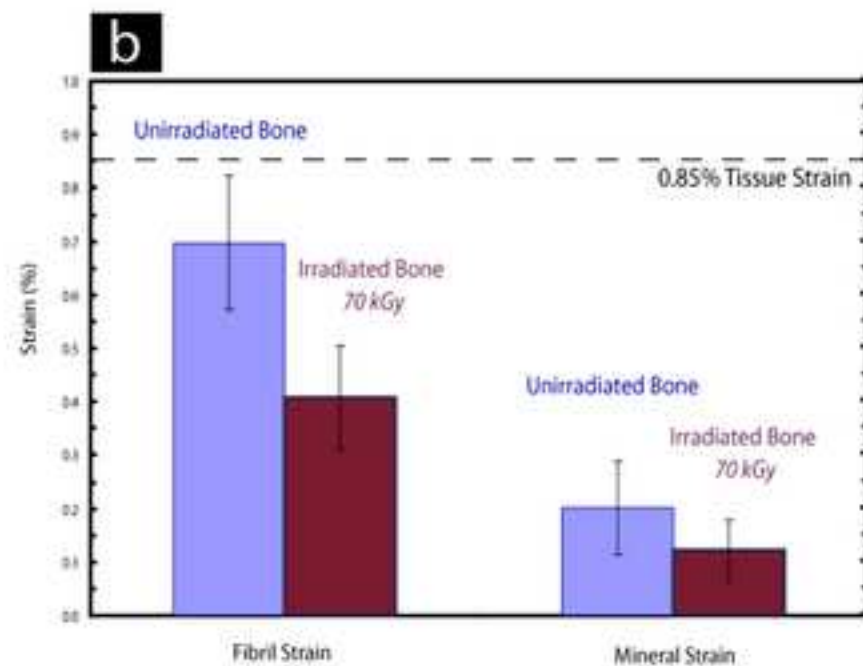
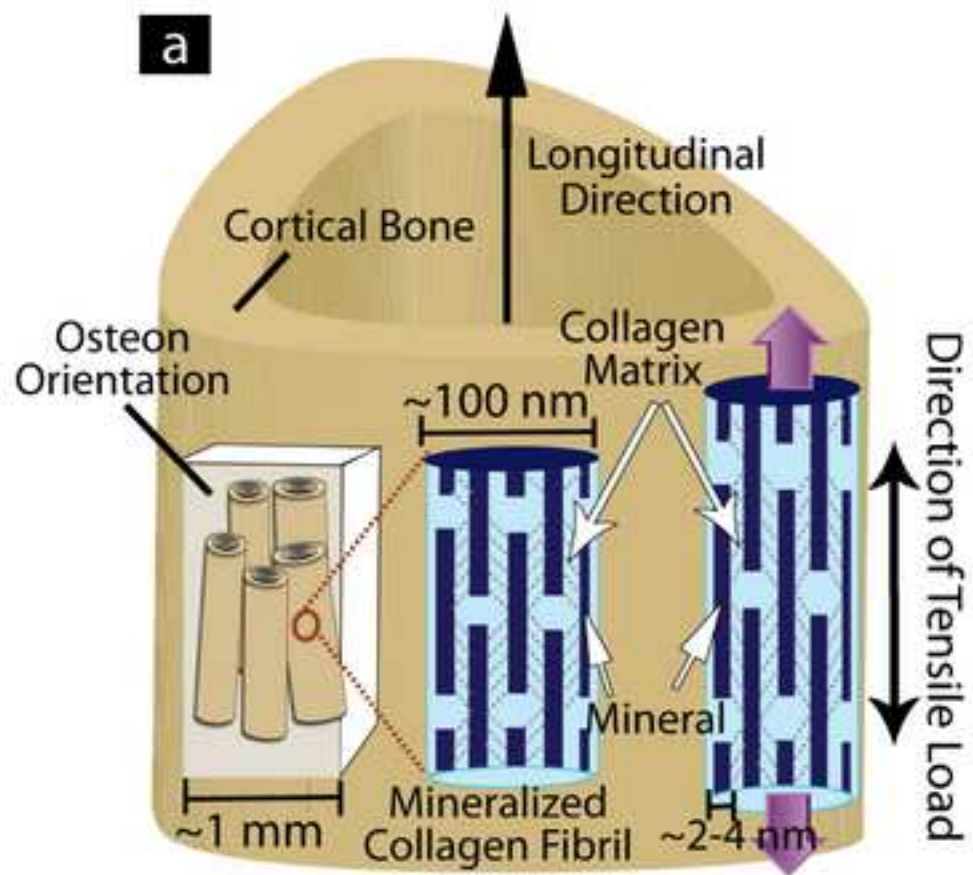


Figure 8
[Click here to download high resolution image](#)

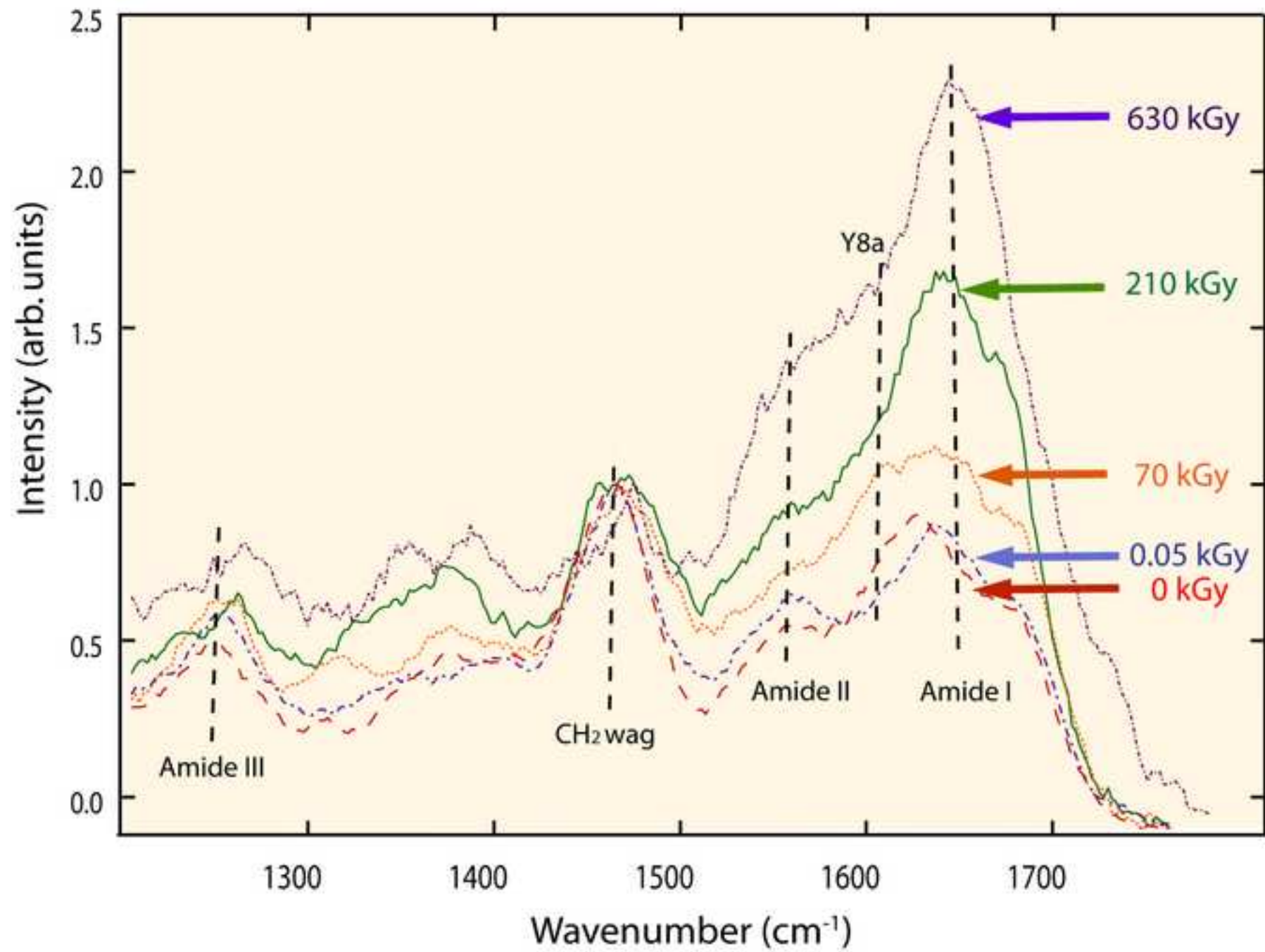


Figure 9
[Click here to download high resolution image](#)

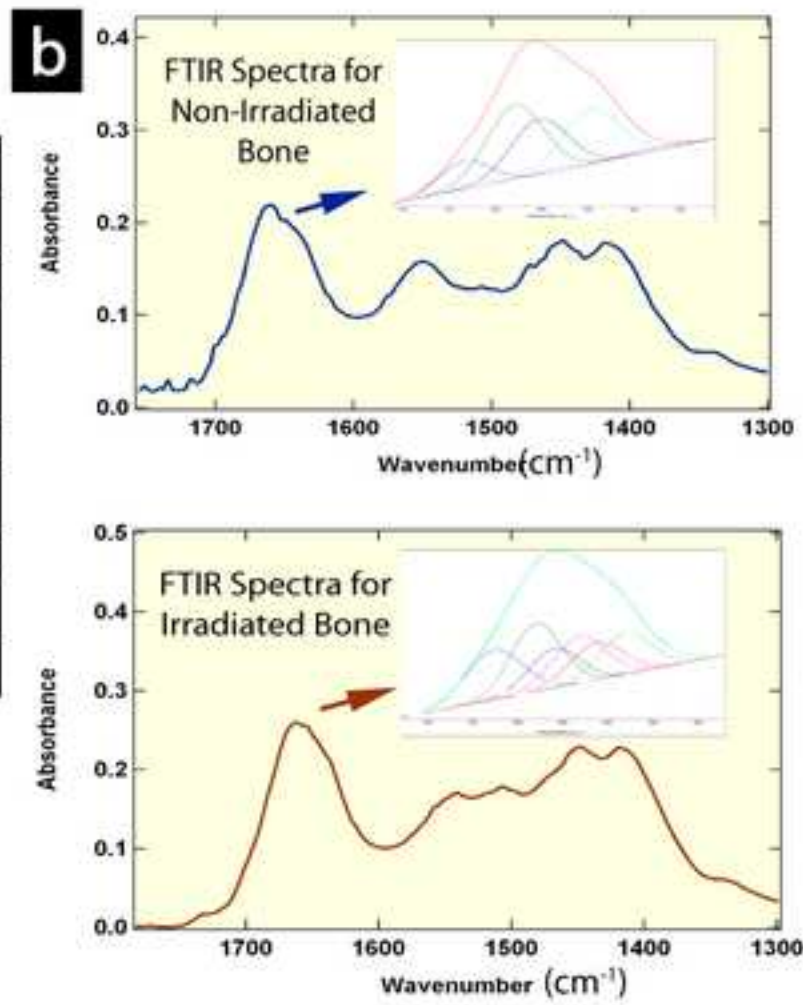
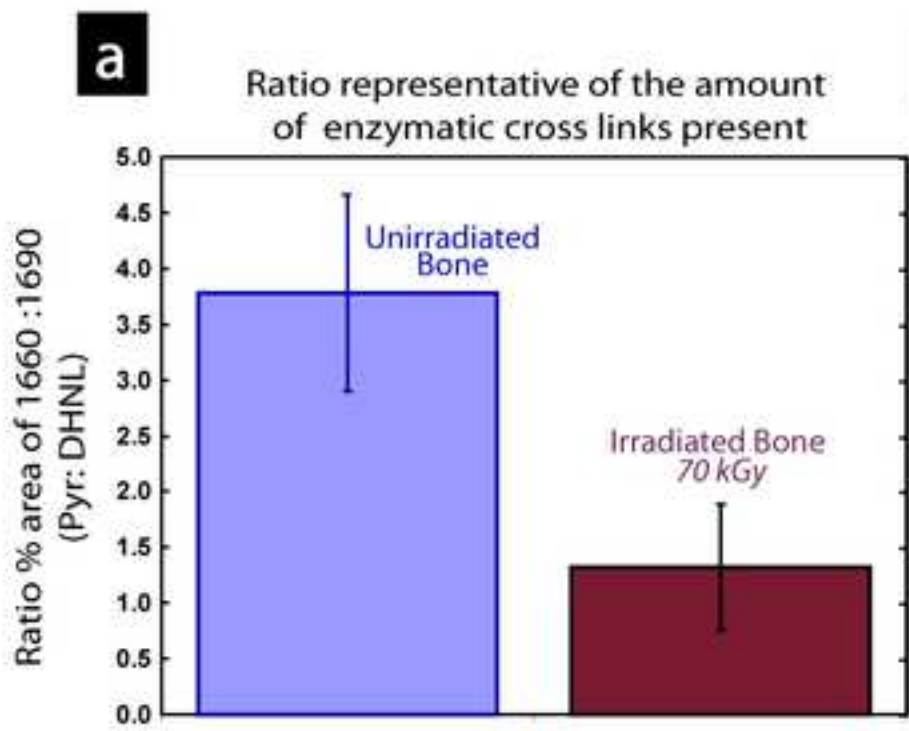
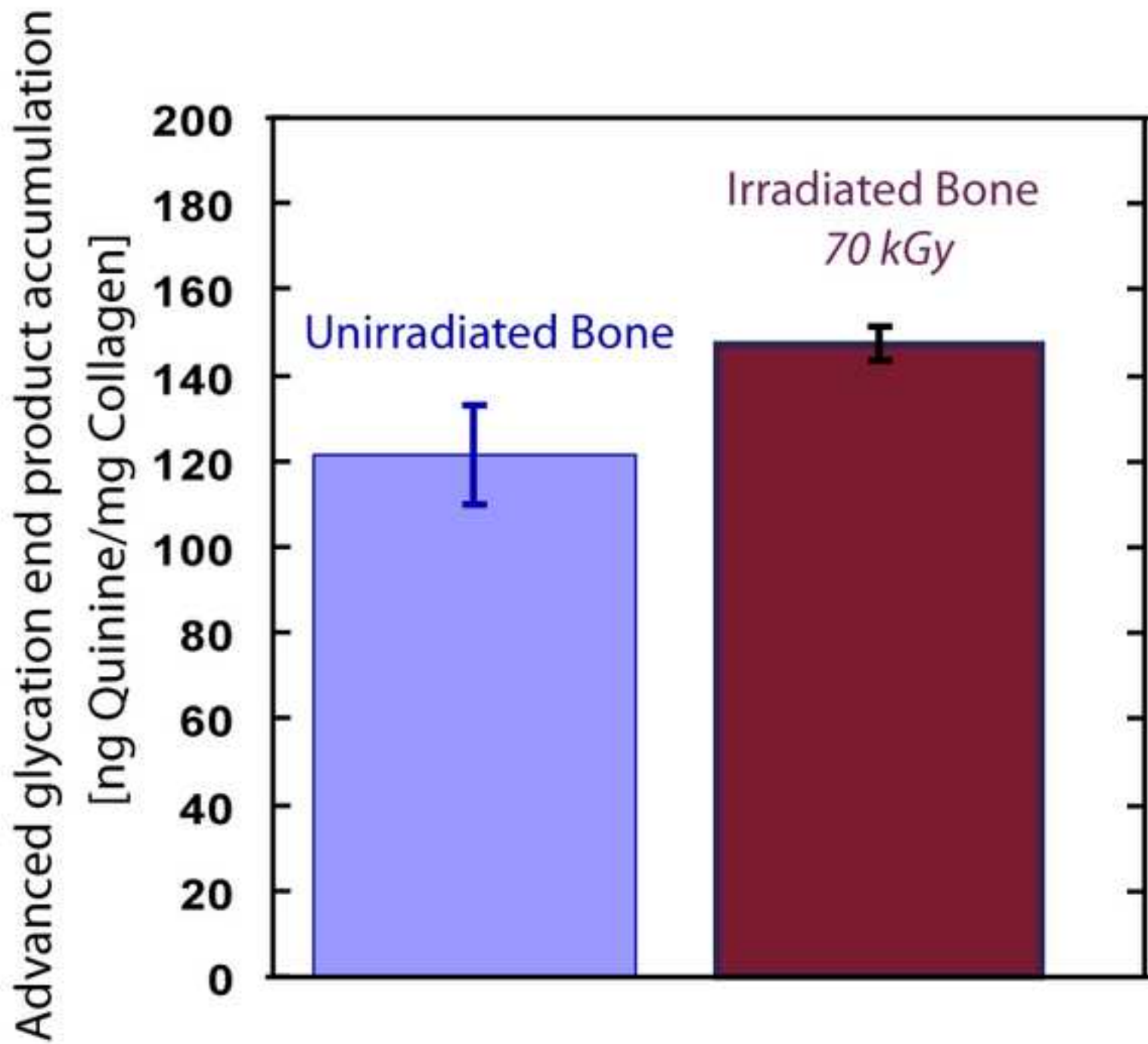


Figure 10
[Click here to download high resolution image](#)



DISCLAIMER

This document was prepared as an account of work sponsored by the United States Government. While this document is believed to contain correct information, neither the United States Government nor any agency thereof, nor the Regents of the University of California, nor any of their employees, makes any warranty, express or implied, or assumes any legal responsibility for the accuracy, completeness, or usefulness of any information, apparatus, product, or process disclosed, or represents that its use would not infringe privately owned rights. Reference herein to any specific commercial product, process, or service by its trade name, trademark, manufacturer, or otherwise, does not necessarily constitute or imply its endorsement, recommendation, or favoring by the United States Government or any agency thereof, or the Regents of the University of California. The views and opinions of authors expressed herein do not necessarily state or reflect those of the United States Government or any agency thereof or the Regents of the University of California.